Major and trace element characterization of Oceanic Anoxic Event 1d (OAE 1d): Insight from the Umbria-Marche Basin, central Italy

Gambacorta, G. [1], Bottini, C. [1], Brumsack, H.-J. [2], Schnetger, B. [2], Erba E. [1]

[1] Dipartimento di Scienze della Terra, Università degli Studi di Milano, Milan, Italy

[2] Institute for Chemistry and Biology of the Marine Environment (ICBM), University of Oldenburg, Oldenburg, Germany

Corresponding author: Gabriele Gambacorta. E-mail address: gabriele.gambacorta@guest.unimi.it. Telephone number: +39 02503 15530

Abstract

The Pialli Level in the Umbria-Marche Basin (central Italy) correlates with the lowermost part of the positive carbon isotopic excursion characterizing the late Albian–early Cenomanian Oceanic Anoxic Event 1d (OAE 1d). High-resolution litho-, bio- and chemostratigraphic data from the Monte Petrano and Le Brecce sections allow for a bed-by-bed comparison of the two successions, and discriminate local from basin-scale signals. We present new X-ray fluorescence, ICP-MS and TOC data for both the limestones and the Pialli Level shales integrated with available carbonate carbon isotopes and nannofossil temperature and nutrient indices. Data indicate a homogenous background sedimentation dominated by pelagic carbonates, biogenic silica with little contribution by clays. The limited variation in lithogenic elements points to an essentially homogeneous detrital source area with limited fluvial terrigenous input. Higher Mn concentrations coupled with low enrichments in redox-sensitive elements, such as U, Fe, S, Re, Mo, Ag, suggest that the Pialli Level shales represent temporary suboxia without reaching anoxia. Furthermore, P, authigenic Ba, Cd and Ni enrichments, together with nannofossil nutrient index indicate generally low primary productivity conditions along the entire succession, with only minor increases for some of the black-to-dark grey shales of the Pialli Level. The nannofossil temperature index highlights a warm climate during the OAE 1d, with the warmest conditions experienced during the deposition of the Pialli Level shales. During the late Albian, the warm and humid climate was interrupted by brief episodes of relatively warmer and less saline surface waters ensuring slower rates of bottom water renewal and producing temporary suboxic conditions. Such paleoceanographic dynamics would be the continuation of episodic warmer and humid pulses characterizing the late Albian interval in the Umbria-Marche Basin. As such, the Pialli Level can be considered the result of a last episode closing a cycle before the establishment of a steadier climate during the early Cenomanian.

Key-words: Albian, Cretaceous, dysoxia, calcareous nannofossils, Pialli Level, trace metals

1. Introduction

The late Albian time interval was marked by important paleoceanographic changes associated with the progressive opening of the Atlantic Ocean and the formation of new gateways and seaways (Giorgioni et al., 2015). The unstable circulation mode that characterized the oceans during the Albian was abandoned in favor of more stable conditions associated to a well-established thermocline and better developed surface and bottom currents across interconnected basins (Giorgioni et al., 2015). As an effect, sedimentation in pelagic settings changed from the black shale-rich and carbonate-poor facies of the Albian to the widespread chalky, black shale-poor facies deposited starting in the late Albian (Giorgioni et al., 2015). In the earliest phase of these chalk-dominated ocean a perturbation of the global carbon cycle occurred across the Albian–Cenomanian boundary interval. This Oceanic Anoxic Event (OAE) 1d is characterized by a long positive $\delta^{13}C$ excursion of about 1‰ (Arthur et al., 1990; Wilson and Norris, 2001). More than 30 years ago, Bréheret (1988) identified an upper Albian organic-carbon enriched horizon, named

Breistroffer Level in the Vocontian Trough. Since then, other organic-rich black shales that correlate with OAE 1d have been described in many other basins (Arthur et al., 1990; Wilson and Norris, 2001). In fact, the OAE 1d carbon isotope anomaly has been identified worldwide in variable depositional settings, thus suggesting a potential global extent of this event. In particular, it has been widely recognized in the western Tethys Ocean (Erbacher and Thurow, 1997; Gale et al., 1996; Stoll and Schrag, 2000; Strasser et al., 2001; Bornemann et al., 2005; Reichelt, 2005; Sprovieri et al., 2013; Gambacorta et al., 2015; Giorgioni et al., 2015; Bąk et al., 2016; Gyawali et al., 2017), in the eastern Tethys Ocean (Vahrenkamp, 2013; Zhang et al., 2016; Wohlwend et al., 2016; Hennhoefer et al., 2018; Yao et al., 2018; Navidtalab et al., 2019), in the northern Tethys (Melinte-Dobrinescu et al., 2015), in the Atlantic Ocean (Wilson and Norris, 2001; Nederbragt et al., 2001; Petrizzo et al., 2008; Ando et al., 2010), in the Pacific Ocean (Takashima et al., 2004; Robinson et al., 2008; Navarro-Ramirez et al., 2015; Rodriguez-Cuicas et al., 2019, 2020), in the Western Interior Seaway (North America) (Gröcke et al., 2006; Gröcke and Joeckel, 2008; Scott et al., 2013; Richey et al., 2018), in the Boreal Realm (Mitchell et al., 1996; Bornemann et al., 2017), and in the Indian Ocean (Madhavaraju et al., 2015).

In order to characterize OAE 1d in western Tethys, we studied the Monte Petrano and Le Brecce pelagic sections in the Umbria-Marche Basin (central Italy), both nicely exposed and with an available high-resolution bio- and chemostratigraphic calibration (Gambacorta et al., 2015). Furthermore, the use of two coeval sections from the same basin allows to discriminate local from basin-scale signals. In the Umbria-Marche Basin OAE 1d is represented by a $\delta^{13}C_{carb}$ increase of 0.7‰ (Gambacorta et al., 2015) and is associated with the so-called Pialli Level (Coccioni, 2001; Coccioni and Galeotti, 2003), an interval characterized by discrete black-to-dark grey shale layers. In this study, the long- and short-term variations in paleoenvironmental conditions characterizing the evolution of OAE 1d are reconstructed at high resolution by means of lithostratigraphy, C-isotope chemostratigraphy, major and trace element geochemistry, and calcareous nannofossils. In particular, we aim to: (1) identify variations in the depositional conditions across the Pialli Level; (2) understand sediment redox history; (3) estimate how primary productivity and calcareous phytoplankton fertility varied across the event; (4) propose a coherent depositional model for the organic-rich layers of the Pialli Level.

2. Geological setting and studied sections

The studied sections are located in the Central Apennines. The Monte Petrano section lies close to the Moria village (Schwarzacher, 1994; Giorgioni et al., 2012; Gambacorta et al., 2015, 2016), while Le Brecce outcrop is located about 3 km west of the Piobbico village (Gambacorta et al. 2015, 2016) (Figs. 1 and 2). The analyzed successions were deposited in the Western Tethys in a basins and swells setting (Alvarez, 1990; Cosentino et al., 2010) on the continental crust of the Adria microplate in the northern tropical climatic belt (Dercourt et al., 2000; Skelton et al., 2003) (Fig. 1). Here, the Scaglia Bianca Formation (Coccioni and Galeotti, 2003; Gambacorta et al., 2015), of late Albian – early Turonian age, consists of calcilutites resulting from lithification of nannofossil-planktonic foraminiferal oozes (Gambacorta et al., 2015), with layers enriched in siliceous radiolarian tests deposited at estimated water depth of about 1500-2000m (Gambacorta et al., 2015).

The studied interval covers the members W1 and W2 (sensu Coccioni and Galeotti, 2003) of the Scaglia Bianca Formation, with the Pialli Level falling entirely within member W1 (Gambacorta et al., 2015) (Fig. 3). From base to top, the 'Lower Yellowish-Grey member' (W1) is mainly characterized by yellowish-grey limestones with nodules and lenses of greenish-grey chert, while the 'Reddish member' (W2) is formed by pink to reddish micritic limestones.

3. Material and methods

The sections investigated for this study were described in earlier studies by Gambacorta et al. (2014, 2016). These authors described sedimentology, texture and composition variations, and sedimentary structures in detail. A total of 73 limestone samples, with a sampling rate of 0.5 m, and 6 black-to-dark grey shales were collected from the Monte Petrano section, while 42 limestone samples, with a sampling rate of about 0.5 m, and 6 black-to-dark grey shales were collected from Le Brecce section. Sampling was done on fresh surfaces in order to minimize weathering effects.

The total organic carbon content (TOC) in the black-to-dark grey shales was determined as the difference of total carbon measured using an elemental analyzer (euro EA Euro Vector®) and carbonate carbon measured by infrared detection after acidification (multi EA 2000, Analytik Jena®). Analytical precision is better than 2% except for samples with <0.1% TOC.

All the recovered samples, both limestones and black-to-dark grey shales, were analyzed by X-ray fluorescence analysis (XRF) at the University of Oldenburg. About 700 mg of sample powder were mixed with 4200 mg lithium tetraborate, pre-oxidized in oven at 500°C overnight with NH_4NO_3 and then fused to glass beads. The beads were analyzed by a wave-length dispersive X-ray fluorescence (WD-XRF) spectrometer equipped with a rhodium tube (Axios Plus, Panalytical®). XRF measurements are based on a calibration with 56 international reference samples covering a wide range in sediment composition. Precision was checked by two in-house standards Peru-1 (fine-grained sediment taken from the upwelling area of the Peruvian margin) and PS-S (Lower Jurassic Posidonia Shale). Analytical precision is better than 1% for Si, Ti, Al, Fe, Mg, Mn, Ca, K, P, Sr, 2% for Ba, Cr, Cu, Mo, Ni, Rb, V, Zn, Zr, and better than 5% for the following minor and trace elements Na, Ga, Nb, Y, except As, Co, Pb (5-10%).

The twelve black-to-dark grey shale samples were also measured for minor and trace elements using inductively coupled plasma-mass spectrometry (ICP-MS). The ICP-MS analysis was conducted at the University of Oldenburg. Powdered sediment samples (50 mg) were pre-oxidized overnight with 1 ml HNO_3 (65%) in polytetrafluoroethylene (PTFE) vessels, and then digested by heating to 180 °C for twelve hours in PTFE autoclaves (PDS-6) with 3 ml HF (40%) and 1 ml $HClO_4$ (70%). Subsequently, acids were evaporated on a hot plate at 180 °C and then the digestions were fumed-off three-times with 6 M HCl. Acid digestions were dissolved in 25 ml HNO_3 (2% v/v), spiked with In and Be as internal standards, and then measured using an ICP-MS (iCAP Q, Thermo Fisher Scientific®). Trueness and precision of the analyses was verified using several in-house reference materials calibrated to international standards. In particular, checks were done on in-house standards previously analyzed by XRF; to check trueness for those elements which could not be measured with XRF, in-house standards were used together with international reference materials after being acid-digested in the same way as the samples. The limestone samples were not analyzed by ICP-MS due to the extremely low concentrations in trace elements as a result of the dilution by the very high calcium content.

Elemental concentrations were normalized to Al in order to account for dilution effects. Concentrations are compared relative to the reference average crustal rocks or average shale (AS) element abundance of Wedepohl (1971, 1991) and expressed as element enrichment (EF_{elem}). Enrichment factors were computed using the following formula:

$$EF_{elem} = (\text{element}/\text{Al})_{samp} \,/\, (\text{element}/\text{Al})_{AS} \quad (1)$$

where $(\text{element}/\text{Al})_{samp}$ is the ratio between the element and aluminum content in a sample, and $(\text{element}/\text{Al})_{AS}$ is the ratio between the element and aluminum abundance in the average shale. Rare-earth elements (REE) concentrations were normalized with respect to Average Post-Archaean Australian Shale (PAAS) concentrations (Taylor and McLennan, 1985). We consider an $EF_{elem} > 3$ as a detectable enrichment and an $EF_{elem} > 10$ a moderate to strong authigenic enrichment (e.g., Tribovillard et al., 2006; Algeo and Tribovillard, 2009). Similarly, we interpret an $EF_{elem} < 0.7$ as a detectable depletion and an $EF_{elem} < 0.1$ as a moderate to strong authigenic depletion. Element enrichment above “normal” detrital background is expressed as element excess ($element_{xs}$) using the following formula:

$$[element]_{xs} = [element]_{samp} - (element/Al)_{bg} \times [Al]_{samp} \quad (2)$$

where $(element/Al)_{bg}$ is the ratio between element and Al in the background detrital flux, chosen, as described in Perkins et al. (2008), as the linear regression slope fitting the element versus Al_2O_3 concentration ratios. The possible bias of using aluminum to normalize elemental concentrations in different lithologies, and the limit of using proxies developed for shales on carbonates, was minimized by integrating a multitude of proxies for describing and interpreting each process.

Calcareous nannofossil temperature (TI) and nutrient (NI) indices were calculated starting from the nannofossil relative abundances obtained counting at least 300 specimens in each sample (from Bottini and Erba, 2018). Counts were performed in simple smear slides under polarized microscope at 1250X magnification. The TI and NI were obtained using the formula of Bottini et al. (2015) who modified the TI and NI of Herrle et al. (2003) as follows:

$$TI = (Ss + Ef + Rp)/(Ss + Ef + Rp + Ra + Zd) \times 100 \quad (3)$$

$$NI = (Bc + Dr + Ze)/(Bc + Dr + Ze + Wb) \times 100 \quad (4)$$

Where Ss: *S. stradneri*; Ef: *E. floralis*; Rp: *R. parvidentatum*; Ra: *R. asper*; Zd: *Z. diplogrammus*; Bc: *B. constans*; Dr: *D. rotatorius*; Ze: *Z. erectus*; Wb: *W. barnesiae*. When the TI reaches the full scale (TI=0), corresponding to maximum warming, we took into account the relative abundances of the warm-water species *R. asper* to trace temperature fluctuations under warm climatic conditions.

4. Results

4.1. Lithostratigraphy

The studied successions are continuous and do not present evidence of slumps, structural discontinuities or sediment reworking by gravity flows, with the sole exception of the interval around 16.0–16.5 m of Le Brecce section that is partly covered by rubble and characterized by a few small faults. Minor evidence of bottom current activity was described by Gambacorta et al. (2016). The Monte Petrano and Le Brecce outcrops in the lowermost part of the section, from 0.0 to 5.5 m and 0 to 3.5 m, respectively, are characterized by alternating pinkish and yellowish grey limestones to marly limestones and marlstones (Fig. 3). The following interval is mainly composed of yellowish grey limestones and marlstones. In correspondence of this part of the succession, in the interval that goes from about 8.80 to 15.35 m in the Monte Petrano section and 6.30 to 12.90 m in Le Brecce section, six black-to-dark grey shales correspond to the Pialli Level. These blackish layers are here named from bottom to top using MP1 to MP6 for the Monte Petrano section and BR1 to BR6 for Le Brecce section (Fig. 3). The Pialli Level black-to-dark grey shales are not evenly spaced, with those from MP2 to MP5 and BR2 to BR5 clustered in less than 2 meters. Moreover, three of them are not discrete black shales but are shading into a brownish marly layer: in particular, the dark grey shale MP1 (at 8.80 m) and BR5 (at 10.05 m) are overlain by a marlstone, while the MP2 (at 10.98 m) has at its base a brownish marlstone. Further up in both sections a very thin black shale seam was observed at 22.13 m and 16.67 m at Monte

Petrano and Le Brecce, respectively. It is important to notice that all the black-to-dark grey shales, with the sole exception of the black shale seams, occur in the lowermost part of the OAE 1d carbon isotopic anomaly. At about 23 m at Monte Petrano and 18 m at Le Brecce section a main lithological change occurs, with the shift to the pinkish limestones and marly limestones associated with the presence of grey-to-pinkish-reddish chert bands of member W2 sensu Coccioni and Galeotti (2003).

4.2. Total organic carbon (TOC)

Analyzed samples have generally low TOC content, with values ranging from 0.1 to 2.5% total weight (tw), with a common trend in organic carbon content in both sections (Fig. 3, Appendixes A and B). In fact, the lowermost two black shales (MP1, MP2 and BR1 and BR2) are characterized by very low values from 0.1 to 0.6% tw, with the lowermost values reached in correspondence of samples MP2 and BR2. The upper black shale MP3 shows a higher TOC content of 1.8% tw, while at Le Brecce sample BR3 has a value of 0.5% tw. Black shales MP4, MP5 and BR4, BR5 are characterized by higher TOC values, ranging from 2.3–2.5% in the Monte Petrano section and 1.4–1.7% tw in Le Brecce section, with samples MP5 and BR5 representing the organic carbon-richest samples. The TOC content then decreases back to values of 0.5 and 0.1% tw in the uppermost black shales MP6 and BR6, respectively. It should be noted that similarly low values were observed also in the directly underlying Albian black-to-dark grey shales recovered in the Piobbico Core, where a TOC content varying between 0.1% and 1.5% tw was documented (Pratt and King, 1986).

4.3. Major and trace elements geochemistry

Average major and trace element concentrations, element/Al, standard deviation (1 σ) and maximum values of the analyzed limestone samples and black-to-dark-grey shale samples for the Monte Petrano section are reported, respectively, in Tables 1a, 1b and

Supplementary material (Appendixes A and B). Moreover, results for the limestones and black-to-dark grey shales samples for Le Brecce section are reported in Tables 2a, 2b.

Enrichment factors based on average shale (AS) values (Wedepohl, 1971, 1991) of all the analyzed limestone samples show for some elements an enrichment. In particular, limestone samples from Monte Petrano (Tab. 1a) are enriched in Ca (EF=315.8), Ba (EF=11.9), Mn (EF=12.1), Pb (EF=5.2), Sr (EF=22.8). For the limestone samples from Le Brecce section (Tab. 2a), the average composition is quite similar to Monte Petrano, with samples strongly enriched in Ca (EF=260.0), Ba (EF=7.5), Mn (EF=12.5) and Sr (EF=18.7). The black-to-dark grey shales samples from the Monte Petrano section (Tab. 1b) are strongly enriched in Ca (EF=91.0), Zn (EF=77.3), Bi (EF=49.9), Cd (EF=59.1), Re (EF=210.5). Evidence of enrichment were observed also for Ba (EF=10.7), Co (EF=9.5), Cu (EF=9.6), Ni (EF=6.2), Sr (EF=10.4), V (EF=7.5), Bi (EF=7.6). Analyzed samples on average are also depleted in Na (EF=0.4). In comparison to AS, black-to-dark grey shale samples of Le Brecce section are strongly enriched in Ca (EF=83.6) and Ag (EF=26.3), and enriched in Ba (EF=6.6), Cu (EF=11.6), Sr (EF=10.1), V (EF=6.2), Bi (EF=8.6), Cd (EF=11.9), Re (EF=24.7). As observed for the Monte Petrano samples, analyzed black-to-dark grey shales of Le Brecce section are depleted in Na (EF=0.4). The enrichment factors for each black-to-dark grey shales in both the sections are plotted in Figure 4.

The average REE patterns of the analyzed samples for the black-to-dark grey shales at Monte Petrano and Le Brecce sections are shown in Figure 5. All samples show a similar REE pattern, with the light REEs (LREE) characterized by a pronounced Ce depletion, a hump for the medium REEs (MREE), while the heavy REEs (HREE) show a weak depletion relative to the MREEs. The REE pattern is depleted compared to PAAS, with an average factor of about 0.4 within the studied interval.

4.4. Nannofossil indices

Calcareous nannofossil assemblages were quantified to obtain percentages of the temperature- and fertility-related taxa in the Monte Petrano and Le Brecce sections (Bottini and Erba, 2018) (Appendixes A and B). The TI and NI reconstructed in both sections are suggestive of paleoclimatic and paleoecological changes throughout OAE 1d interval (Figs. 6 and 7). At Monte Petrano (Fig. 6) the NI indicates relatively high surface water fertility conditions in the interval preceding OAE 1d. The onset of OAE 1d is preceded by a decrease in the NI that remains low in the early phase of the event (up to 14.6 m) except for higher NI values detected in black shales MP3, MP4 and MP5 and in correspondence of the sample between MP3 and MP4. The middle and late OAE 1d (from 15 to 20 m) is characterized by relatively higher fertility with peaks indicating slightly mesotrophic conditions during black shale MP6 deposition and the samples right below and above it. Similar higher fertility was obtained for samples at 18 m and at 19.5 m. After OAE 1d, the NI shows a progressive decrease. The largest contribute to higher NI values comes from *Biscutum constans* (20-30%) which is the dominant mesotrophic species while *Discorhabdus rotatorius* and *Zeugrhabdotus erectus* show percentages below 10% (Bottini and Erba, 2018).

In the Monte Petrano section, the TI indicates relatively cooler conditions prior to OAE 1d followed by a warming pulse (at ca. 6 m) just preceding the OAE 1d onset (Fig. 6). Warm conditions are reconstructed during OAE 1d with many samples having TI= 0 (corresponding to highest temperatures). The relative abundance of *R. asper* (Bottini and Erba, 2018) (Figs. 6, 7 and Supplementary material) suggests that highest temperatures where reached prior to and at black shale MP1 and in the interval comprised between black shale MP2 and MP5. The TI suggests a relative cooling in the interval between 23 and 29 m, above OAE 1d. A decrease of the TI towards warmer climate is detected around 30 m upwards. At Monte Petrano the warm-water nannofossil species *R. asper* is relatively abundant (ca. 10-20%) while cold-water taxa such as *Repagulum parvidentatum*, *Staurolithites stradneri* and *Eprolithus floralis* are very rare (< 1%) (Bottini and Erba, 2018).

At Le Brecce (Fig. 7) the NI indicates higher surface water fertility prior to OAE 1d. The onset of OAE 1d is preceded by a decrease in the NI and lowest values are reached during the early phase of the event, including black shales BR1 and BR2 also marked by low fertility. The interval comprised between black shale BR2 and BR5 shows four NI spikes corresponding to the sample just above black shale BR2, the black shale BR3, the sample above it and the sample below black shale BR5. The black shales BR4 and BR5 are characterized by low NI values. Higher surface water fertility is detected during the middle and late OAE 1d (from 11 to 16 m), except for black shale BR6 marked by relatively low fertility. The uppermost part of the studied interval (17–20 m) is characterized by decreasing NI values. As for the Monte Petrano section, the most abundant mesotrophic species at Le Brecce is *B. constans* which reaches ca. 20-30% in the intervals of higher fertility (Bottini and Erba, 2018).

The TI of Le Brecce section (Fig. 7) suggests cooler temperatures prior to OAE 1d. A relative warming precedes the OAE 1d onset and warmer temperatures characterize the OAE 1d up to its end. Relative cooling spikes correspond to black shale BR1, the sample above it, the sample below black shale BR3 and black shale BR3. A minor temperature decrease is recorded after OAE 1d from 19 to 20 m. As for Monte Petrano, *R. asper* is the most abundant warm water species (ca. 10%) while cold water species *R. parvidentatum*, *S. stradneri* and *E. floralis* are very rare (Bottini and Erba, 2018).

5. Discussion

5.1. Stratigraphic correlation

Based on integrated litho-, bio-, and chemostratigraphic data (Gambacorta et al., 2015; Gilardoni, 2017) a high-resolution stratigraphic correlation of the two studied successions is presented in Figure 3. According to the sole nannofossil biostratigraphy, both sections encompass a single biozone NC10a (Gambacorta et al., 2015), while several planktonic foraminiferal zones were identified (Gilardoni, 2017). The stratigraphic resolution is improved by combining chemo- and lithostratigraphy. In fact, on the basis of the shape and absolute values of the carbon isotope excursion, together with the lithological changes – that include a shift in color in the limestone layers from pinkish to yellowish grey, the presence of chert bands – it is possible to set a one-to-one correlation of the various black-to-dark grey shales forming the Pialli Level. According to high-resolution litho-, bio- and chemostratigraphy, we estimate a ~3 m gap at Le Brecce in the faulted interval at about 16.5 m. In fact, we observe that the values reached by the $\delta^{13}C_{carb}$ curve in the interval above peak 'b' of the OAE 1d anomaly at Le Brecce are too low to be considered as part of the complete OAE 1d carbon isotopic excursion. First, the carbon isotope profile is characterized by a sharp decrease in values around 16.5 m, and second, the carbon isotope profile never reaches the values of about 3‰ registered at peak 'c' in the Monte Petrano section. The last occurrence (LO) of *Ticinella* sp., located at about 24.0 m at Monte Petrano and at about 19.2 m at Le Brecce (Gilardoni, 2017), further confirms that part of the record is missing at Le Brecce. By taking into account such a gap, we obtain a good lithostratigraphic correlation for both the transition from the W1 to the W2 member and a correspondence of the occurrence of the black shale seams in the two sections.

5.2. Sediment geochemistry

The observed lithological variations are reflected in the major and trace element contents. Stratigraphic distributions of lithogenic conservative elements for the Monte Petrano and Le Brecce sections are reported in the Supplementary material (Appendixes C and D). Elemental compositions are plotted on a triangular diagram with axes Al_2O_3, SiO_2, and CaO in order to show the variation in the three major components of sedimentary rocks, i.e. clays, quartz and/or biogenic silica, and calcium carbonate respectively (Fig. 8). Most samples from both sections plot below the so-called 'carbonate dilution line' connecting the

AS point to the pure carbonate end-member, with a general shift towards high SiO_2 content. This graph suggests a stable and homogenous background sedimentation dominated by pelagic carbonates, biogenic silica with little contribution by detrital clays, except most of the MP and BR samples originating from the Pialli Level. The composition of the upper Albian – lower Cenomanian Scaglia Bianca samples is consistent with what is described for the "mid" to upper Cenomanian Scaglia Bianca limestones of the Furlo section in the Umbria-Marche Basin (Turgeon and Brumsack, 2006).

The Ti and Zr concentrations are considered as proxies for coarse-to-medium grained detrital input (e.g. Cox et al., 1995; Schneider et al., 1997; Ganeshram et al., 1999; Sageman and Lyons, 2005), while Rb and K, are interpreted as indicative of the finer grained fraction. In particular, Rb substitutes K in aluminosilicate minerals (Heinrichs et al., 1980; Calvert and Pedersen, 2007), while K is mainly associated with K-feldspars and clay minerals, in particular with the chemically stable illite (Cox et al., 1995). The average composition of all the analyzed samples for Ti, K, Fe, Rb, Zr is quite similar to AS values (Wedepohl, 1971, 1991) (Fig. 9 and Tabs. 1a, 1b, 2a, 2b), thus giving no evidence of enrichment or depletion in comparison to AS. These elements, considered as lithogenic elements (Koinig et al., 2003) express an essentially homogeneous detrital source area through time, with limited terrigenous detrital input in a low-energy distal depositional setting. We speculate that the source area was probably located at least 1000 km north of the Umbria-Marche Basin, based on the reconstruction of Giorgioni et al. (2015). The low detrital supply likely resulted in a poor to no dilution of the organic matter fraction, as supported by the TOC/Al variation (Figs. 6 and 7). The higher TOC/Al ratio of black-to-dark grey shales MP3/BR3, MP4/BR4 and MP5/BR5 suggests probable higher preservation of TOC during the deposition of those layers.

Aeolian inputs to marine sediments can be estimated using geochemical proxies such as Si/Al, Ti/Al and Zr/Al ratios (Schnetger, 1992; Schnetger er al., 2000). Available data show a good correlation of Si, Ti and Zr concentrations with the fine-grain size proxies such as Al, K and Rb, suggesting transport of both fine- and coarse- to medium-grained fractions. The absence of evidence of a grain-size sorting typical of the aeolian deposits (Wang et al., 2017) let us infer a dominant riverine contribution for the origin of the terrigenous input. Furthermore, we point out that the bell-shape REE pattern of the analyzed black-to-dark grey shales (Fig. 5), characterized by an enrichment in the MREEs, is similar to the REE composition of the dissolved load of numerous rivers (Elderfield et al.,1990). For this reason, we suppose mainly a fluvial origin of the siliciclastic input, even if a partial influx from an aeolian source cannot be excluded.

The geochemical composition of sediments can be used to trace the provenance of the siliciclastic detrital fraction (e.g., Taylor and McLennan, 1985; Cullers, 2000; Basu et al., 2016; Nagarajan et al., 2017; Zaid et al., 2018). The Al_2O_3/TiO_2 ratio is used to determine original source rock composition, being not influenced during moderate chemical weathering and diagenesis (Garcia et al., 1994). This ratio has an average and almost constant value of about 23.5 in both sections, thus suggesting an origin of the detrital fraction of typical upper continental crust composition (Hayashi et al., 1997). The low Na_2O content observed both in the limestone and shale samples is likely due to the preferential chemical weathering of plagioclase on the earth surface and in a missing Na-rich clay mineral in the terrigenous environment. However, a contribution from a plagioclase-poor source material cannot be excluded.

5.3. Paleotemperature variations

Diagenesis acting on sediments during burial can strongly affect the original oxygen isotope signal. In fact, due to fractioning associated with variations in temperature and presence of burial fluids, the precipitation of isotopically homogeneous cements occurs (e.g. Anderson and Arthur, 1983; Marshall 1992; Rodríguez-Cuicas et al., 2019). In order to estimate the degree of the post-depositional diagenetic imprint, a cross-plot of $\delta^{13}C_{carb}$ data against the $\delta^{18}O_{carb}$ values for the analyzed samples was used (Fig. 10). As no significant correlation is observed in the data (R^2 = 0.001 and R^2 = 0.096 for the Monte Petrano and Le Brecce section, respectively) we assume that no significant effect of diagenesis on the oxygen isotope record occurred. In both sections, the $\delta^{18}O_{carb}$ curve is characterized by generally low values, thus indicating mostly warm conditions (Gambacorta et al., 2015), with a common shift towards lower $\delta^{18}O_{carb}$ values occurring approximately at the lowermost black-to-dark grey shale layer of the Pialli Level (Figs. 6 and 7). In particular, across the OAE 1d, the $\delta^{18}O_{carb}$ curve is characterized by the lowest values associated with an additional negative shift of about 0.5‰. This can be either interpreted as evidence of warmer conditions or as the delivery of fresh waters into the basin.

The nannofossil TI is in good agreement with oxygen isotopes since a warming trend is evidenced by both proxies at Monte Petrano and Le Brecce (Figs. 6 and 7). Cooler conditions are associated with the lowermost part of the studied record (Interval 1, from 0.0 to 6.0 m and 0.0 to 4.0 m at the Monte Petrano and Le Brecce, respectively), followed by a shift to warmer temperatures in Interval 2 (from about 6.0 to 22.5 m at Monte Petrano, and from about 4.0 to 17.0 m at Le Brecce). A relative shift to cooler temperatures (Interval 3) takes place at about 22.5 m at Monte Petrano and at the stratigraphically equivalent depth of 17.0 m at Le Brecce. A return to warmer conditions follows in the uppermost part of the Monte Petrano section (Interval 4, from about 30.0 to 35.0 m).

According to these data, the deposition of the black-to-dark grey shales of the Pialli Level occurred under the warmest phase of the studied stratigraphic interval. However, at Le Brecce, black shales layers BR1 and BR3 were deposited at temporary relatively cooler conditions.

5.4. Paleoredox conditions

Concentrations in redox-sensitive elements of the analyzed samples (Tabs. 1a, 1b, 2a, 2b, and Figs. 4, 6 and 7) were used as proxies for sediment paleo-oxygen conditions (Brumsack, 1980; Algeo and Maynard, 2004; Brumsack, 2006; Lyons and Severmann, 2006; Tribovillard et al., 2006; Calvert and Pedersen, 2007; Piper and Calvert, 2009; Little et al., 2015).

Manganese is scavenged from the water column under oxic conditions, mainly forming the insoluble Mn-oxyhydroxides MnO_2 and MnOOH. However, being Mn very mobile under reducing settings, it is easily removed from sediments under anoxic conditions. As a consequence, it escapes back to the water column when not trapped in authigenic Mn-carbonates (Hild and Brumsack, 1998; Calvert and Pedersen, 1993; Brumsack, 2006; Tribovillard et al., 2006). The high Mn/Al ratio in all limestone samples (EF_{Mn} up to 25) indicates that they deposited under oxic conditions as no Mn loss occurred. Although with values greater than AS, the Mn/Al ratio is lower in black-to-dark grey shales (EF_{Mn} around 3) (Table 3) suggesting that some Mn diffused back from sediments to the water column under low oxygen conditions. It must be noted that Mn may reside in carbonates also in the form of non-oxide minerals, thus potentially resulting in high Mn concentrations even under suboxic to anoxic conditions. However, the integration with other redox-sensitive proxies confirms that the studied carbonates deposited under oxic conditions.

Some redox fluctuations are found for black-to-dark grey shales based on trace metal concentrations (Figs. 4, 6 and 7). In particular, lower shales MP1, MP2 at Monte Petrano and BR1, BR2 at Le Brecce and the topmost shales MP6 and BR6 do not show enrichments in any other redox-sensitive elements, thus suggesting an oxic depositional environment (Crusius et al., 1996; Algeo and Maynard, 2004; Brumsack, 2006; Lyons and Severmann, 2006; Tribovillard et al., 2006) (Tabs. 1a, 1b, 2a, 2b, and Figs. 4, 6 and 7). At least suboxic redox conditions can be inferred for the black-to-dark grey shales MP3, MP4 and MP5 at Monte Petrano and BR3, BR4 and BR5 at Le Brecce as these samples are characterized by an enrichment in V, Cd, Ag and Re (Algeo and Maynard, 2004; Tribovillard et al., 2006) (Table 3). Vanadium is reduced from V(V) to V(IV) under mild reducing conditions, forming vanadyl ions (VO^{2-}), hydroxyl species and insoluble hydroxides (Tribovillard et al., 2006). Under the presence of free H_2S, it is further reduced to V(III). Cadmium is released from degrading organic material, and if sulfate reduction is occurring will form CdS in the presence of even minute concentrations of H_2S in micro-domains (Boyle et al., 1976; Bruland, 1980; Rosenthal et al., 1995; Tribovillard et al., 2006). This is further confirmed by the high Ag content, which has a similar sensitivity to H_2S as Cd, thus indicating high input of organic matter and traces of H_2S in the pore fluids (Crusius and Thomson, 1993; Brumsack, 2006; McKay and Pedersen, 2008). The high Re content and low Mo concentrations further confirm that only suboxic conditions were reached (Crusius et al., 1996; Algeo and Maynard, 2004; Tribovillard et al., 2006; Scheiderich et al., 2010; Scott and Lyons, 2012) (Fig. 11). In fact, while Re can be easily enriched under suboxic settings, the removal of Mo into sediments occurs under more reducing conditions with the presence of free H_2S (Crusius et al., 1996; Tribovillard et al., 2006). Redox conditions experienced by samples BR3, BR4 and BR5 at Le Brecce sections were milder than their time-equivalent shales at Monte Petrano. Although sections are only a few kilometers apart and at similar paleo-water depths, the minor changes in the paleoredox state might derive from slight differences in bathymetry. For these samples Mn/Al is on the AS level or higher, with quite lower enrichments in Cd or Re, which means that sulfate reduction and traces of H_2S were low (Figs. 4, 6 and 7). However, the slight increase in V, Re, Cd and Ag in the black-to-dark grey shales BR3, BR4 and BR5 suggest that these layers experienced suboxic conditions.

Additional indication on the paleoredox conditions can be inferred by comparing redox-sensitive element variations versus TOC content (Algeo and Maynard, 2004) (Appendix E). In fact, Algeo and Maynard (2004), by analyzing core shales from the Kansas City Group, defined thresholds for the covariation between redox-sensitive elements and

TOC for discriminating different regimes in redox conditions. Al-normalized elemental composition versus TOC of the analyzed black-to-dark grey shales further confirms that true anoxia was never reached. In particular, all the samples fall within the suboxic field with Monte Petrano experiencing relatively stronger redox conditions. Uranium contents comparable to AS also support this interpretation as severe anoxic conditions are needed for its accumulation (Algeo and Maynard, 2004; Tribovillard et al., 2006). The lack of enrichment in other elements associated with a stronger redox state, such as Fe and S, further implies that truly anoxic conditions were never reached. It is important to point out that observed enrichment in some other redox-sensitive elements, such as As, Ni, Co, Cu, are not necessarily associated with severe anoxic conditions, but are more likely controlled by their scavenging by Mn-oxides and hydroxides (Tribovillard et al., 2006).

5.5. Paleoproductivity conditions

Many authors have proposed the use of TOC as indicator of paleoproductivity (Pedersen and Calvert, 1990; Canfield, 1994; Tyson, 2005; Zonneveld et al., 2010; Schoepfer et al., 2015), although, being a large part of the organic matter re-mineralized, the final TOC content often represents only a small percentage of the amount of the organic matter produced (Canfield, 1994; Tyson, 1995). As a consequence, the low TOC content of analyzed black-to-dark grey shales (from about 0.1 to 2.5% in weight) (Figs. 6 and 7) does not necessarily imply a low organic matter flux in the water column.

Redox conditions in the depositional environment have a strong effect on accumulation and preservation of elemental productivity proxies (Pedersen and Calvert, 1990; Lochte et al., 2003; Avert and Paytan, 2004; Anderson and Winkler, 2005; Tribovillard et al., 2006; Schoepfer et al., 2015), thus in some cases hindering their use as tracers for biological productivity. However, as reducing conditions were mild during the deposition of the studied successions, the impact of such a behavior on the record was limited. In particular, total phosphorous, Ba_{xs}, Ni and Cd were used to infer changes in paleoproductivity.

Total phosphorous, a fundamental nutrient for marine phytoplankton, can be considered, with good approximation, representative of the organically-derived P (Ingall et al., 2005; Tribovillard et al., 2006; Schoepfer et al., 2015). The P export through the water column is closely related to the organic matter associated with plankton and bioapatite, with only a limited contribution from the detrital fraction (Algeo and Ingall, 2007; Schoepfer et al., 2015). Our data indicate fairly constant P/Al ratios in Monte Petrano and Le Brecce sections, with EF_P values of about 3.2-3.9 both in the limestones and in the black-to-dark grey shale layers (Figs. 4, 6 and 7, and Tabs. 1a, 1b, 2a, 2b) suggesting generally low primary productivity conditions if compared with phosphorous EF´s of 5 to 40 observed in modern high productivity upwelling areas (Brumsack, 2006). However, phosphorous recycling in the 1500-2000m water column (Gambacorta et al., 2015) or at the sediment/water interface (Tribovillard et al., 2006; Algeo and Ingall, 2007) might have affected the studied record.

Ba_{xs} can be used as a reliable productivity indicator (e.g., Brumsack and Gieskes, 1983; Brumsack, 1986, 1989; Dymond et al., 1992; McManus et al., 1998; Gingele et al., 1999; Babu et al., 2002; Paytan and Griffith, 2007; Liguori et al., 2016) under oxic conditions (Dehairs et al., 1980; Schoepfer et al., 2015) at sites where water depth is higher than 1000 m (Babu et al., 2002). Ba is a less reliable paleoproductivity proxy under reducing conditions, in particular in the case of intense sulfate reduction, as it becomes mobile (Dymond et al., 1992; Torres et al., 1996; Tribovillard et al., 2006). Ba_{xs} was computed using a Ba/Al background value of 79 $\times 10^{-4}$ and 55 $\times 10^{-4}$ for the Monte Petrano and Le Brecce sections, respectively (see Table 4). In the studied successions Ba_{xs} peaks are present for most black-to-dark grey shales at Monte Petrano with the only exception of sample MP6 (Tabs. 1a, 1b, 2a, 2b and Figs. 7 and 8). At Le Brecce, only black-to-dark grey shales BR1 and BR2 are characterized by higher Ba_{xs} contents. The relative distance of the two sections to rivers, as sources of Ba to the basin, cannot be considered as the main driver for explaining observed variations in Ba content. First, river water is strongly diluted by seawater when entering the ocean, thus indicating a limited impact of riverine inputs on Ba concentration in coastal seawater, and thus on the composition of the sediment (Martin and Meybeck, 1979; Bruland, 2014). Second, as the source area was probably located about 1000 km north of the studied sections, the hypothesis of a direct control of rivers on observed variations in Ba concentration seems not reliable. However, observed differences in Ba_{xs} content between time-equivalent black-to-dark grey shales may partially reflect some local variations in productivity conditions. Indeed, as at the time of deposition the two sections were closely located, the effect of post-depositional diagenetic processes on measured Ba concentrations cannot be excluded.

Further indications are provided by redox-sensitive elements Ni and Cd, which exhibit a nutrient-like behavior in the water column (Nozaki, 2001). These micronutrients are transported together with the organic matter from the surface ocean to the seafloor (Tribovillard et al., 2006). In the studied samples (Tabs. 1a, 1b, 2a, 2b) the Ni/Al ratio and Cd/Al show higher values in MP3, MP4 and MP5 shales at Monte Petrano and BR4 and BR5 at Le Brecce.

The nannofossil NI, being redox independent, can be used as an indicator of paleofertility conditions of surface waters (e.g. Herrle et al., 2004; Bornemann et al., 2005; Bottini and Erba, 2018). The NI curves at Monte Petrano and Le Brecce display similar trends indicative of the following surface water fertility conditions (Figs. 6 and 7): a) prior to OAE 1d fertility was relatively high; b) a drop towards lower fertility occurred just before OAE 1d onset and characterized the early part of the event; c) the interval between shales MP2/BR2 and MP5/BR5 shows fertility increases detected at, or close to, black shales MP3/BR3, MP4/BR4 and MP5/BR5; d) a progressive increase in fertility is detected in the late OAE 1d, followed by e) a gradual decrease of fertility after OAE 1d. Regarding the black-to-dark grey shale layers, assuming the NI value of 35 as the boundary separating oligotrophic from mesotrophic conditions, higher fertility is associated only to black shales MP6 and BR3 (Figs. 6 and 7).

Therefore, the patterns of the geochemical proxies for paleoproductivity and the nannofossil NI are similar, indicating a low productivity/fertility in the lower part of OAE 1d and higher values for MP3/BR3, MP4/BR4 and MP5/BR5 (Figs. 6 and 7). However, the NI displays a fertility relative increase above the Pialli Level in the upper part of OAE 1d.

In addition to the above described proxies, the interpretation of the contribution from biogenic material is further supported by considering the depletion in Ce observed in all black-to-dark grey shales (Fig. 5). In fact, relative variations in Ce can be related to changes in redox conditions of the depositional environment via changes in the oxidation state of the cerium (Bodin et al., 2013), but also to the contribution of the biogenic fraction grown in equilibrium with the Ce-depleted oceanic surface water (Elderfield and Greaves, 1982; McLennan, 1989; Pattan et al., 2005; Akagi et al., 2011). If the terrigenous fraction is very low compared to the biogenic fraction, the sediment can mirror the REE pattern of the surface seawater. However, generally the REE content in the pure carbonate fraction is lower by several orders of magnitude compared to the terrigenous fraction. The black-to-dark grey shales consist of about 75% biogenic fraction (carbonate, apatite, baryte, biogenic silica – on average about 34% of the silica content is in excess in the black-to-dark grey shales). It could be shown that even 1-2% of shale contamination by terrigenous material can affect the REE patterns of limestones (Nothdurft et al., 2004). Therefore, the Ce depletion in studied samples might be partly ascribed to its loss via diffusing pore water to the sediment seawater boundary under reducing conditions. The relatively flat REE patterns, with the exception of the pronounced Ce depletion, further support that productivity conditions were low at both sites. This is confirmed by the suite of geochemical proxies, although relative increases are associated to deposition of layers MP3, MP4, MP5 and BR3, BR4, BR5, with relatively higher productivity at Monte Petrano. To conclude, the negative Ce-anomaly seems more related to the reducing conditions during black and grey shale deposition than a primary signal from the surface water.

It should be also noted that both limestones and black-to-dark grey shales contain relatively high amounts of SiO_2 (Figs. 4, 8 and 9, and Tabs. 1a, 1b, 2a, 2b) as indicated on the average EF_{Si} from 1.4 to 3.5, with about 50% of the silica content in excess in both sections (computed using a Si/Al background value of 3.95 and 4.30 for the Monte Petrano and Le Brecce sections respectively, see Table 4). This suggests also a contribute from biogenic quartz. In particular, black-to-dark grey shales BR5 and BR6 are characterized by high Si concentrations, with an EF_{Si} equal to 5.51 and 7.97 respectively.

5.6. Comparison with published elemental and calcareous nannofossil data

Very few publications report estimates of paleoenvironmental conditions during OAE 1d by means of elemental geochemical data. Bornemann et al. (2017) measured by XRF core scanning two cores from an upper Albian – lower Cenomanian shaly succession from the Lower Saxony Basin. They interpreted the most negative Mn/Fe values as indicator of suboxic conditions in correspondence of the lowermost part of OAE 1d in the Boreal Realm (Fig. 12). There, the presence of intense bioturbation and only limited dark grey and well-laminated intervals can be considered a further evidence of absence of truly anoxic conditions. Anoxia, reconstructed on the basis of elemental data, is reported exclusively for two successions deposited in peculiar proximal settings. Scott et al. (2013) studied a section deposited on a nearshore muddy marine shelf below wave base in the Chihuahua Trough (New Mexico). On the basis of Fe enrichment and Mn depletion, they interpret the low TOC (between 0.3 and 0.7% wt) shales of the OAE 1d as deposited in an iron-rich anoxic environment that never turned euxinic. Rodriguez-Cuicas et al. (2019) investigated a succession deposited in a tidal-dominated deltaic system in southwestern Venezuela.

Enrichments in U, V, Mo, Cr, Ni and Zn were interpreted as indicative of anoxic and possibly euxinic conditions for intervals with TOC values up to 10%. Moreover, U-Mo and Mo-TOC co-variation patterns were considered symptomatic of semi-restricted basinal setting with poor water circulation (Rodriguez-Cuicas et al. 2019). The $\delta^{13}C$ chemostratigraphy of the New Mexico (Scott et al. 2013) and Venezuela (Rodriguez-Cuicas et al. 2019) sections are quite different from other records and do not show the typical positive anomaly characteristic of OAE 1d at global scale (e.g., Gale et al., 1996; Mitchell et al., 1996; Wilson and Norris, 2001; Nederbragt et al., 2001; Gambacorta et al., 2015; Bornemann et al., 2017). Thus, the black shale interval within the *Rotalipora appenninica* Zone might not be equivalent of the Pialli or the Breistroffer Levels.

Calcareous nannofossil data across OAE 1d are available for the Vocontian Basin (France) and Blake Nose (ODP Site 1052, Atlantic Ocean) (Fig. 12). At Col de Palluel, Vocontian Basin, Bornemann et al. (2005) studied the nannofossil content of the Main Breistroffer Level – corresponding to black shale 2 and 3 of the Breistroffer Level (sensu Bréheret et al., 1997) – and evidenced generally higher fertility conditions punctuated by lower fertility pulses in correspondence of the black shale layers. The temperature reconstructed on the basis of $\delta^{18}O$ data and nannofossil TI through the Main Breistroffer Level (Bornemann et al., 2005) are indicative of warm conditions with a minor decrease in the topmost part of the Main Breistroffer Level. In the Blieux section from the Vocontian Basin, calcareous nannofossils were investigated across the Breistroffer Level (Giraud et al., 2003), but the absence of carbon isotope stratigraphy hampers a straightforward correlation to the Col de Palluel section as well as other sections. The lowermost part of the Breistroffer Level is marked by an increase in fertility-related species that decline in its upper part and then increase again above the Breistroffer Level. The fertility-relates taxon *B. constans* is generally higher in abundance at the Col de Palluel (30–45%) and Blieux (25–45%) compared to our studied sections (5–30%), suggesting generally higher trophic conditions in the Vocontian Basin compared to the Umbria-Marche Basin. At Blake Nose (ODP Site 1052) the nannofossil NI indicates a decrease in fertility at the onset of OAE 1d followed by an increase in the upper part of the $\delta^{13}C$ anomaly (Watkins et al., 2005). At ODP Site 1052, the abundance of *B. constans* (5–25 %) is similar to that found in the Umbria-Marche Basin. Thus, available nannofossil data show analogies between the Central Atlantic (Blake Nose) and Western Tethys (Umbria-Marche Basin) with a decrease in fertility at OAE 1d onset and during its early phase followed by an increase toward the end of the C isotopic anomaly. Conditions in the Vocontian Basin were, instead, generally mesotrophic, hence apparently reversed relative to both Blake Nose and Umbria-Marche Basin. This discrepancy is further evidenced by a lower fertility regime in the black shales of the Breistroffer Level relative to the intervening marlstones at Col de Palluel (Bornemann et al., 2005).

5.7. Depositional processes across OAE 1d in the western Tethys

The comparison of the Pialli Level black-to-dark grey shales in the two studied sections, even with some minor variations presumably related to local factors, reveals common patterns in basin-scale processes during OAE 1d. However, it must be noted that the Pialli Level does not represent the lithological expression of the entire OAE 1d, since it corresponds exclusively to the lower part of the positive carbon isotope excursion (Fig. 3).

The late Albian – early Cenomanian time interval was characterized by an alternation of relatively cooler and warmer climatic conditions, in a period of generally warm temperatures (O’Brien et al., 2017; Bottini and Erba, 2018). As testified by the temperature-related nannofossil taxa measured in the Monte Petrano and Le Brecce records, warmer conditions established during the entire OAE 1d, with relative further warming during the sedimentation of the Pialli Level black-to-dark grey shales (Figs. 6 and 7). A global warm climate during the OAE 1d is documented in a variety of settings (Bornemann et al., 2005;

Retallack, 2009; Arens and Harris, 2015; Melinte-Dobrinescu et al., 2015; Bottini and Erba, 2018; Richey et al., 2018; Ovechkina et al., 2019). Retallack (2009), by analyzing paleosols and cuticles from the Cedar Mountain Fm. in Utah, showed evidence of a hot and humid climatic phase with high precipitation during the OAE 1d time interval. Similarly, anomalous precipitations and warm temperatures were described by Arens and Harris (2015) based on the analysis of leaf margin and area of the Soap Creek Flora of the Cedar Mountain Formation. Richey et al. (2018), applying stomatal- and plant isotope-based estimates deduced an average increase in $p\mathrm{CO_2}$ that led to a global temperature increase of about 2°C during OAE 1d. Warmer conditions and increased CO_2 might be related to volcanism associated to the emplacement of the late Albian (about 99 Ma) Hess Rise in the Pacific Ocean (Eldholm and Coffin, 2000; BouDagher-Fadel, 2015) and/or of the central portion of the Kerguelen Plateau large igneous province (Erba, 2004; Richey et al., 2018).

Warmer conditions resulted in an enhanced thermocline able to weaken water mass vertical mixing (Fig. 13). The humid regime that likely accompanied the warm climate, induced an accelerated weathering and runoff, as testified by a higher input of fine-grained siliciclastics (most MP and BR black-to-dark grey shale samples are depleted in carbonate, as shown in Figure 8) reflected by the lithological change from limestones to the Pialli Level shales. The increased input of fresh water produced a pycnocline further lessening vertical mixing resulting in a lower oxygen content of the deep water. In the Umbria-Marche Basin, primary productivity was generally low during OAE 1d, with small peaks for the Pialli Level shales MP3, MP4 and MP5 at Monte Petrano and the time-equivalent shales BR3, BR4 and BR5 at Le Brecce section (Figs. 6 and 7). Variations in organic matter fluxes, presumably, were not then the main driver of the deposition of the black-to-dark grey shales of the Pialli Level. Organic matter was mostly degraded along the water column resulting in low TOC in black-to-dark grey shales. Moreover, the sediment/water interface became suboxic but never reached truly anoxic conditions, as testified by the observed high Mn concentrations and limited enrichments in redox-sensitive elements.

Metal accumulation was also favored by biogeochemical cycles and by Mn-oxides and hydroxides shuttling. The higher Mn contents, likely delivered at higher rate by fluvial input, might have exerted an important control on the observed composition in redox-sensitive elements with dominating oxygenated bottom waters (Calvert and Pedersen, 1996). A contribution from terrigenous organic matter cannot be excluded. This organic matter, being less subjected to degradation, would have been more easily preserved under oxic conditions with limited impact on sediment redox state.

The Pialli Level is not stratigraphically equivalent to the Breistroffer Level (Fig. 12), further emphasizing the role of local conditions on dysoxia-anoxia as also demonstrated for other OAEs (e.g. Tsikos et al., 2004). A similar depositional model was proposed for the upper Albian rhythmic black shales of the Piobbico core in the Umbria-Marche Basin by Tiraboschi et al. (2009) that shortly precede the Pialli Level. Combined oxygen isotope composition and nannofossil data suggested the development of density stratification of water masses and strengthened pycnocline occurred under generally warm and oligotrophic conditions (Tiraboschi et al., 2009). A contribution to these upper Albian black shales from a continental organic matter input is testified by the low hydrogen content and the presence of abundant wood debris, spores, pollen and freshwater algae (Pratt and King, 1986; Fiet, 1998). The black shales of the Pialli Level, therefore, would represent a continuation or a temporary resumption of warm and humid throbbing preceding a steadier climatic regime persisting during the early Cenomanian.

6. Conclusions

During the late Albian–early Cenomanian the depositional environment in the Umbria-Marche Basin was dominated by pelagic calcareous oozes with a minor contribution by siliceous oozes and low fine-grained detrital input. Data indicate that the terrigenous contribution was mainly supplied to the studied area by rivers, from a homogeneous distant source area some 1000-1200 km north of the Umbria-Marche Basin after erosion of rocks with a typical upper continental crust composition. The late Albian long-term sea-level rise promoting better connections between basins was possibly an effective driver for attenuation of the terrigenous input to coastal settings, while had a negligible influence on distal areas such as the Umbria-Marche Basin. In the lowermost part of the OAE 1d $\delta^{13}C_{carb}$ excursion of about 0.7‰, identified at both Monte Petrano and Le Brecce sections, six black-to-dark grey shale layers represent the uppermost Albian Pialli Level. Geochemical and nannofossil data indicate low primary productivity conditions during the OAE 1d interval, with a minor increase observed within the central part of the Pialli Level that is followed by generally more fertile surface waters. The nannofossil temperature index shows generally warm conditions across OAE 1d with a warming peak during the deposition of the Pialli Level. Warming resulted in an enhancement of the thermocline partially affecting water mass mixing efficiency. Increased humidity triggered enhanced runoff, promoting the fine-grained siliciclastic input recorded in the Pialli Level shales, and contributed to the establishment of a pycnocline. Results indicate that preservation of organic material was the main driver for black shale deposition, but variations in productivity resulted in different TOC amount associated to individual black-to-dark grey shale. The limited amount of organic matter that reached the seafloor was mostly degraded along the water column, with negligible effects on sediment redox conditions as shown by the high Mn concentrations coupled with limited enrichments in redox-sensitive elements in the Pialli Level.

The late Albian was the time of onset of the Cretaceous super-warming culminating with the early Turonian Thermal Maximum (O'Brien et al., 2017). In the Umbria-Marche Basin, recurrent warmer and more humid conditions were reached during the deposition of black shales within the Pialli Level: relatively warmer and less saline surface waters weakened O_2 absorption and vertical mixing, resulting in slower rates of deep-water renewal and consequent suboxia. Combined geochemical and nannofossil proxies indicate that productivity variations were irrelevant for deposition of the Pialli Level black shales.

A similar model was reconstructed for older Late Albian dysoxic-anoxic episodes in the Umbria-Marche Basin (Tiraboschi et al., 2009), thus the black shales of the Pialli Level represent a last episode of intermittent warmer and humid conditions before the establishment of a steadier climate during the early Cenomanian.

Acknowledgments

The authors are grateful to the Editor Don Porcelli for his helpful suggestions, and to Jean-Carlos Montero-Serrano and two anonymous Reviewers that with their valuable comments contributed to improve the quality of the manuscript. The research was conducted within the PRIN 2017RX9XXXY awarded to EE.

Data availability

Datasets related to this article can be found at https://data.mendeley.com/datasets/vfcv9nrmgm/draft?a=508d6193-52d3-47bb-8578-acf3c0b95d5d an open-source online data repository hosted at Mendeley Data. Supplementary material consists of: two tables with major and trace element data and nannofossil indices for the two sections; two figures reporting the stratigraphic distribution of lithogenic conservative elements (Si, Ti, K, Fe, Rb, Zr) versus Al at Monte Petrano and Le Brecce sections; crossplots reporting Al-normalized redox-sensitive elements composition (Cu, Ni, Cr, Co, Mo, U, V, Zn, Pb) versus TOC for the black-to-dark grey shale layers at Monte Petrano and Le Brecce sections.

References

Akagi, T., Fu., F., Hongo, Y., Takahashi, K., 2011. Composition of rare earth elements in settling particles collected in the highly productive North Pacific Ocean and Bering Sea: Implications for siliceous-matter dissolution kinetics and formation of two REE-enriched phases. Geochimica et Cosmochimica Acta 75, 4857–4876.

Algeo, T.J., Maynard, J.B., 2004. Trace-element behavior and redox facies in core shales of Upper Pennsylvanian Kansas-type cyclothems. Chemical Geology 206, 289–318.

Algeo, T.J., Ingall, E., 2007. Sedimentary Corg:P ratios, paleocean ventilation, and Phanerozoic atmospheric pO_2. Palaeogeography, Palaeoclimatology, Palaeoecology 256, 130–155

Algeo, T.J., Tribovillard, N., 2009. Environmental analysis of paleoceanographic systems based on molybdenum–uranium covariation. Chemical Geology 268, 211–225.

Alvarez, W., 1990. Pattern of extensional faulting in pelagic carbonates of the Umbria–Marche Apennines of central Italy. Geology 18, 407–410.

Anderson, T., Arthur, M., 1983. Stable isotopes of oxygen and carbon and their application to sedimentologic and paleoenvironmental problems. Stable isotopes in sedimentary geology 10, 1–151.

Anderson, R., Winckler, G., 2005. Problems with paleoproductivity proxies. Paleoceanography 20, PA3012, doi: 10.1029/2004PA001107.

Ando, A., Huber, O., MacLeod, K.G., 2010. Depth-habitat reorganization of planktonic foraminifera across the Albian/Cenomanian boundary. Paleobiology 36(3), 357–373.

Arens, N.C., Harris, E.B., 2015. Paleoclimatic reconstruction for the Albian–Cenomanian transition based on a dominantly angiosperm flora from the Cedar Mountain Formation, Utah, USA. Cretaceous Research 53, 140–152.

Arthur, M.A., Brumsack, H.-J., Jenkyns, H.C., Schlanger, S.O., 1990. Stratigraphy, geochemistry, and paleoceanography of organic carbon-rich Cretaceous sequences. In:

Ginsburg, R.N., Beaudoin, B. (Eds.), Cretaceous, Resources, Events, and Rhythms: Background and Plans for Research. Kluwer Academic Publishers, Dordrecht, pp. 75–119.

Averyt, K.B., Paytan, A., 2004. A comparison of multiple proxies for export production in the equatorial Pacific. Paleoceanography 19, PA4003, doi:10.1029/2004PA001005.

Babu, C.P., Brumsack, H.-J., Schnetger, B., Böttcher, M.E., 2002. Barium as a productivity proxy in continental margin sediments: a study from the eastern Arabian Sea. Marine Geology 184, 3–4, 189–206.

Bąk, K., Fabiańska, M., Bąk, M., Misz-Kennan, M., Zielińska, M., Dulemba, P., Bryndal, T., Naglik, B., 2016. Organic matter in upper Albian marine sediments in the High-Tatric units, central western Carpathians related to Oceanic Anoxic Event 1d–Geochemistry, microfacies and palynology. Palaeogeography, Palaeoclimatology, Palaeoecology 454, 212–227.

Basu, A., Bickford, M.E., Deasy, R., 2016. Inferring tectonic provenance of siliciclastic rocks from their chemical composition: A dissent. Sedimentary Geology 336, 26–35.

Bodin, S., Godet, A., Westermann, S., Föllmi, K.B., 2013. Secular change in northwestern Tethyan water-mass oxygenation during the late Hauterivian–early Aptian. Earth and Planetary Science Letters 374, 121–131.

Bornemann, A., Pross, J., Reichelt, K., Herrle, J.O., Hemleben, C., Mutterlose, J., 2005. Reconstruction of short-term palaeoceanographic changes during the formation of the Late Albian 'Niveau Breistroffer' black shales (Oceanic Anoxic Event 1d, SE France). Journal of the Geological Society, London 162, 623–639.

Bornemann, A., Erbacher, J., Heldt, M., Kollaske, T., Wilmsen, M., Lübke, N., Huck, S., Vollmar, N. M., Wonik, T., 2017. The Albian–Cenomanian transition and Oceanic Anoxic Event 1d – an example from the Boreal Realm. Sedimentology 64, 44–65.

Bottini, C., Erba, E., 2018. Mid-Cretaceous paleoenvironmental changes in the western Tethys. Climate of the Past 14, 1147–1163.

BouDagher-Fadel, M.K., 2015. Biostratigraphic and Geological Significance of Planktonic Foraminifera. Developments in Paleontology & Stratigraphy 22, Elsevier, Amsterdam, 312 pp.

Boyle, E.A., Sclater, F., Edmond, J.M., 1976. On the marine geochemistry of cadmium. Nature 263, 42–44.

Bréhéret, J.G., 1988. Episodes de sedimentation riche en matiere organique dans les marnes bleues d'age aptien et albien de la partie pelagique du bassin vocontien. Bulletin de la Societe Geologique de France IV, 349–356.

Bruland, K.W., 1980. Oceanographic distributions of cadmium, zinc, nickel, and copper in the North Pacific. Earth and Planetary Science Letters 47, 176–198.

Bruland, K.W., Middag, R., Lohan, M.C., 2013. Controls of Trace Metals in Seawater. In: Mottl, M.J, Elderfield, H. (Eds.), Treatise on Geochemistry. Second Edition, Philadelphia, USA. Saunders, Elsevier Inc., pp. 19–51.

Brumsack, H.-J., 1980. Geochemistry of Cretaceous black shales from the Atlantic Ocean (DSDP Legs 11, 14, 36 and 41). Chemical Geology 31, 1–25.

Brumsack, H.J., 1986. The inorganic geochemistry of Cretaceous black shales (DSDP leg 41) in comparison to modern upwelling sediments from the Gulf of California. In: Summerhayes, C.P., Shackleton, N.J. (Eds.), North Atlantic Palaeoceanography. Geol. Soc. Spec. Publ., vol. 21, pp. 447–462.

Brumsack, H.J., 1989. Geochemistry of recent TOC-rich sediments from the Gulf of California and the Black Sea. Geol. Rundsch. 78, 851–882.

Brumsack, H.-J., 2006. The trace metal content of recent organic carbon-rich sediments: implications for Cretaceous black shale formation. Palaeogeography Palaeoclimatology Palaeoecology 232, 344–361.

Brumsack, H.J., Gieskes, J.M., 1983. Interstitial water trace-element chemistry of laminated sediments of the Gulf of California (Mexico). Mar. Chem. 14, 89–106.

Calvert, S.E., Pedersen, T.F., 1993. Geochemistry of Recent oxic and anoxic marine sediments: Implications for the geological record. Marine Geology 113, 67–88.

Calvert, S.E., Pedersen, T.F., 1996. Sedimentary geochemistory of manganese: implications for the environment of formation of manganiferous black shales. Economic Geology 91, 36–47.

Calvert, S.E., Pedersen, T.F., 2007. Elemental Proxies for Palaeoclimatic and Palaeoceanographic Variability in Marine Sediments: Interpretation and Application, in: Hillaire-Marcel, C., de Vernal, A. (Eds.), Paleoceanography of the Late Cenozoic, Part 1, Methods. Elsevier, New York, pp. 567-644.

Canfield, D.E., 1994. Factors influencing organic carbon preservation in marine sediments. Chemical Geology 114, 315–329.

Coccioni, R., 2001. The “Pialli Level” from the latest Albian of the Umbria-Marche Apennines (Italy). Federazione Italiana di Scienze della Terra, Geoitalia 2001, 192–193.

Coccioni, R., Galeotti, S., 2003. The mid-Cenomanian Event: prelude to OAE 2. Palaeogeography, Palaeoclimatology, Palaeoecology 190, 427–440.

Cosentino, D., Cipollari, P., Marsili, P., Scrocca, D., 2010. Geology of the central Apennines: a regional review, in: Beltrando, M., Peccerillo, A., Mattei, M., Conticelli, S. (Eds.), The Geology of Italy, Journal of the Virtual Explorer 36, paper 11, Electronic Edition.

Cox R., Lowe, D.R., Cullers, R.L., 1995. The influence of sediment recycling and basement composition on evolution of mudrock chemistry in the southwestern United States. Geochimica et Cosmochimica Acta 59, 2919–2940.

Crusius, J., Calvert, S., Pedersen, T., Sage, D., 1996. Rhenium and molybdenum enrichments in sediments as indicators of oxic, suboxic, and sulfidic conditions of deposition. Earth and Planetary Science Letters 145, 65–78.

Crusius, J., Thomson, J., 2003. Mobility of authigenic rhenium, silver, and selenium during postdepositional oxidation in marine sediments. Geochimica et Cosmochimica Acta 67, 265–273.

Cullers, R.L., 2000. The geochemistry of shales, siltstones and sandstones of Pennsylvanian - Permian age, Colorado, U.S.A.: implications for provenance and metamorphic studies. Lithos 51, 181–203.

Dehairs, F., Chesselet,R., Jedwab,K., 1980.Discrete suspended particles of barite and the barium cycle in the open ocean. Earth and Planetary Science Letters 49, 528–550.

Dercourt, J., Gaetani, M., Vrielinck, B., Barrier, E., Biju-Duval, B., Brunet, M.F., Cadet, J.P., Crasquin, S., Sandulescu M., 2000. Atlas of Peri-Tethys, Palaeogeographical Maps. Paris, France: Commission de la Carte Geologique du Monde (CCGN/CGMW).

Dymond, J., Suess, E., Lyle, M., 1992. Barium in deep-sea sediment: a proxy for paleoproductivity. Paleoceanography 7, 163–181.

Elderfield, H., Greaves, M.J., 1982. The rare earth elements in seawater. Nature 296, 214–219.

Elderfield, H., Upstill-Goddard, R., Sholkovitz, E.R.,1990. The rare earth elements in rivers, estuaries, and coastal seas and their significance to the composition of ocean waters. Geochimica and Cosmochimica Acta 54,971–991.

Eldholm, O., Coffin, M.F., 2000. Large igneous provinces and plate tectonics. In: Richards, M.A., Gordon, R.G., van der Hilst, R.D. (Eds.), The History and Dynamics of Global Plate Motions. American Geophysical Union Geophysical Monograph. 121. American Geophysical Union, Washington, DC, pp. 309–326.

Erba, 2004. Calcareous nannofossils and Mesozoic oceanic anoxic events. Marine Micropaleontology 52, 85–106.

Erbacher, J., Thurow, J., 1997. Influence of oceanic anoxic events on the evolution of mid-Cretaceous radiolaria in the North Atlantic and western Tethys. Marine Micropaleontology 30, 139–158.

Fiet, N., 1998. Les black shales, un outil chronostratigraphique haute resolution. Exemple de l'Albien du bassin de Marches-Ombrie (Italie centrale). Bulletin de la Société géologique de France 169, 221–231.

Gale, A.S., Kennedy, W.J., Burnett, J.A., Caron, M., Kidd, B.E., 1996. The Late Albian to Early Cenomanian succession at Mont Risou near Rosans (Drôme, SE France): an integrated study (ammonites, inoceramids, planktonic foraminifera, nannofossils, oxygen and carbon isotopes). Cretaceous Research 17(5), 515–606.

Gambacorta, G., Jenkyns, H.C., Russo, F., Tsikos, H., Wilson, P.A., Faucher, G., Erba, E., 2015. Carbon-and oxygen-isotope records of mid-Cretaceous Tethyan pelagic sequences from the Umbria–Marche and Belluno Basins (Italy). Newsletters on Stratigraphy 48(3), 299–323.

Gambacorta, G., Bersezio, R., Weissert, H., Erba, E., 2016. Onset and demise of Cretaceous oceanic anoxic events: The coupling of surface and bottom oceanic processes in two pelagic basins of the western Tethys. Paleoceanography 31(6), 732–757.

Ganeshram, R.S., Calvert, S.E., Pedersen, T.F., Cowie, G.L., 1999. Factors controlling the burial of organic carbon in laminated and bioturbated sediments off NW Mexico: implications for hydrocarbon preservation. Geochimica et Cosmochimica Acta 63, 1723–1734.

Garcia, D., Fonteilles, M., Moutte, J., 1994. Sedimentary fractionations between Al, Ti, and Zr and the genesis of strongly peraluminous granites. The Journal of Geology 102, 411–422.

Gilardoni, S., 2017. Late Albian-Cenomanian planktonic foraminiferal biostratigraphy, taxonomy and paleoceanographic inferences. PhD thesis, University of Milano, pp. 1–250.

Gingele, F.X., Zabel, M., Kasten, S., Bonn, W.J., Nürnberg, C.C., 1999. Biogenic Barium as a Proxy for Paleoproductivity: Methods and Limitations of Application, in: Fischer, G., Wefer, G. (Eds.), Use of Proxies in Paleoceanography. Springer, Berlin, Heidelberg, pp. 345–364.

Giorgioni, M., Weissert, H., Bernasconi, S.M., Hochuli, P.A., Coccioni, R., Keller, C.E., 2012. Orbital control on carbon cycle and oceanography in the mid-Cretaceous greenhouse. Paleoceanography 27(1), PA1204, doi: 10.1029/2011PA002163.

Giorgioni, M., Weissert, H., Bernasconi, S.M., Hochuli, P.A., Keller, C.E., Coccioni, R., Petrizzo, M.R., Lukeneder, P.A., Garcia, T.I., 2015. Paleoceanographic changes during the Albian–Cenomanian in the Tethys and North Atlantic and the onset of the Cretaceous chalk. Global and Planetary Change 126, 46–61.

Giraud, F., Olivero, D., Baudin, F., Reboulet, S., Pittet, B., Proux, O., 2003. Minor changes in surface-water fertility across the oceanic anoxic event 1d (latest Albian, SE France) evidenced by calcareous nannofossils. International Journal of Earth Sciences 92(2), 267–284.

Gröcke, D.R., Ludvigson, G.A., Witzke, B.L., Robinson, S.A., Joeckel, R.M., Ufnar, D.F., Ravn, R. L., 2006. Recognizing the Albian-Cenomanian (OAE1d) sequence boundary using plant carbon isotopes: Dakota Formation, Western Interior Basin, USA. Geology 34(3), 193–196.

Gröcke, D.R., Joeckel, R.M., 2008. A stratigraphic test of the terrestrial carbon isotope record of the latest Albian OAE from the Dakota Formation, Nebraska. In: Joeckel, R.M., Ludvigson, G.A., Macfarlane, P.A. (Eds.), FIELD TRIP 2: Fluvial-Estuarine Deposition in the Mid-Cretaceous Dakota Formation, Kansas and Nebraska. Kansas Geologic Survey, Lawrence, KS, pp. 24–30.

Gyawali, B.R., Nishi, H., Takashima, R., Herrle, J.O., Takayanagi, H., Latil, J.L., Iryu, Y., 2017. Upper Albian–upper Turonian calcareous nannofossil biostratigraphy and chemostratigraphy in the Vocontian Basin, southeastern France. Newsletters on Stratigraphy 50(2), 111–139.

Hayashi, K., Fujisawa, H., Holland, H., Ohmoto, H., 1997. Geochemistry of ~1.9 Ga sedimentary rocks from northeastern Labrador, Canada. Geochimica et Cosmochimica Acta 61(19), 4115–4137.

Heinrichs, H., Schulz-Dobrick, B., Wedepohl, K.H., 1980. Terrestrial geochemistry of Cd, Bi, Tl, Pb, Zn and Rb. Geochimica et Cosmochimica Acta, 44, 1519–1533.

Hennhoefer, D., Al Suwaidi, A., Bottini, C., Helja, E., Steuber, T., 2018. The Albian to Turonian carbon isotope record from the Shilaif Basin (United Arab Emirates) and its regional and intercontinental correlation. Sedimentology 66, 536–555.

Hild, E., Brumsack, H.-J., 1998. Major and minor element geochemistry of Lower Aptian sediments from the NW German Basin (core Hoheneggelsen KB 40). Cretaceous Research 19, 615–633.

Hu, F., Yang, X., 2016. Geochemical and geomorphological evidence for the provenance of aeolian deposits in the Badain Jaran Desert, northwestern China. Quaternary Science Reviews 131, 179–192.

Ingall, E.D., Kolowith, L., Lyons, T., Hurtgen, M., 2005. Sediment carbon, nitrogen, and phosphorous cycling in an anoxic fjord, Effingham Inlet, British Columbia, American Journal of Science 305, 240–258.

Koinig, K.A., Shotyk, W., Lotter, A.F., Ohlendorf, C., Sturm, M., 2003. 9000 years of geochemical evolution of lithogenic major and trace elements in the sediment of an alpine lake–the role of climate, vegetation, and land-use history. Journal of Paleolimnology 30, 307–320.

Liguori, B.T.P., De Almeida, M.G., De Rezende, C.E., 2016. Barium and its importance as an indicator of (paleo)productivity. Anais da Academia Brasileira de Ciências 88(4), 2093–2103.

Lyons, T.W., Severmann, S., 2006. A critical look at iron paleoredox proxies: New insights from modern euxinic marine basins. Geochimica et Cosmochimica Acta 70, 5698–5722.

Little, S.H., Vance, D., Lyons, T.W., McManus, J., 2015. Controls on trace metal authigenic enrichment in reducing sediments: insights from modern oxygen-deficient settings. American Journal of Science 315 (2), 77–119.

Lochte, K., Anderson, R.F., Francois, R., Jahnke, R.A., Shimmield, G., Vetrov, A., 2003. Benthic processes and the burial of carbon, in: Fasham, M.J.R., Ocean Biogeochemistry: The Role of the Ocean Carbon Cycle in Global Change. Springer, New York, pp. 196–216.

Madhavaraju, J., Sial, A.N., Hussain, S.M., Nagarajan, R., Ramasamy, S., 2015. Petrography and stable isotopic variations in Dalmiapuram Formation of Cauvery Basin, South India: implication on OAE1d. Chinese Journal of Geochemistry 34(3), 447–458.

Marshall, J.D., 1992. Climatic and oceanographic isotopic signals from the carbonate rock record and their preservation. Geological Magazine 129, 143 –160.

Martin, J.-M., Meybeck, M., 1979. Elemental mass-balance of material carried by world rivers. Marine Chemistry 7, 173–206.

McKay, J.L., Pedersen, T.F., 2008. The accumulation of silver in marine sediments: A link to biogenic Ba and marine productivity. Global Biogeochemical Cycles 22, GB4010, doi:10.1029/2007GB003136.

McLennan, S.M., 1989. Rare earth elements in sedimentary rocks: influence of provenance and sedimentary processes. In: Lipin, B.R., McKay, G.A. (Eds.), Geochemistry and Mineralogy of Rare Earth Elements, Reviews in Mineralogy vol. 21. The Mineralogical Society of America, Washington D.C., pp. 169–200.

McManus, J., Berelson, W.M., Klinkhammer, G.P., Johnson, K.S., Coale, K.H., Anderson, R.F., Kumar, N., Burdige, D.J., Hammond, D.E., Brumsack, H.-J., McCorkle, D.C., Rushdi, A., 1998. Geochemistry of barium in marine sediments: implications for its use as a paleoproxy. Geochim. Cosmochim. Acta 62, 3453–3473.

Melinte-Dobrinescu, M.C., Roban, R.D., Stoica, M. 2015. Palaeoenvironmental changes across the Albian-Cenomanian boundary interval of the Eastern Carpathians. Cretaceous Research, 54, 68–85.

Mitchell, S.F., Paul, C.R.C., Gale, A.S., 1996. Carbon isotopes and sequence stratigraphy. Geological Society, London, Special Publications 104(1), 11–24.

Nagarajan, R., Armstrong-Altrin, J.S., Kessler, F.L., Jong, J., 2017. Petrological and geochemical constraints on provenance, paleoweathering, and tectonic setting of clastic sediments from the Neogene Lambir and Sibuti Formations, northwest Borneo, in: Mazumder, R. (Ed.), Sediment Provenance. Elsevier, Amsterdam, pp. 123–153.

Navarro-Ramirez, J.P., Bodin, S., Heimhofer, U., Immenhauser, A., 2015. Record of Albian to early Cenomanian environmental perturbation in the eastern sub-equatorial Pacific. Palaeogeography, Palaeoclimatology, Palaeoecology 423, 122–137.

Navidtalab, A., Heimhofer, U., Huck, S., Omidvar, M., Rahimpour-Bonab, H., Aharipour, R., Shakeri, A., 2019. Biochemostratigraphy of an upper Albian–Turonian succession from the southeastern Neo-Tethys margin, SW Iran. Palaeogeography, Palaeoclimatology, Palaeoecology 533, 109255.

Nederbragt, A.J., Fiorentino, A., Klosowska, B., 2001. Quantitative analysis of calcareous microfossils across the Albian–Cenomanian boundary oceanic anoxic event at DSDP Site 547 (North Atlantic). Palaeogeography, Palaeoclimatology, Palaeoecology 166(3-4), 401–421.

Nothdurft, L.D., Webb, G.E., Kamber, B.S., 2004. Rare earth element geochemistry of Late Devonian reefal carbonates, Canning Basin, Western Australia: confirmation of a seawater REE proxy in ancient limestones. Geochimica et Cosmochimica Acta, 68: 263–283.

Nozaki, Y. 2001. Elemental distribution: Overview. Pp. 840–845 in Encyclopedia of Ocean Sciences, vol. 2. J.H. Steele, S.A. Thorpe, and K.K. Turekian (eds, Academic Press, London, http://dx.doi.org/10.1006/rwos.2001.0402.

O'Brien, C. L., Robinson, S. A., Pancost, R. D., Sinninghe Damsté, J.S.,, Schoutend, S., Lunt, D.J., Alsenz, H., Bornemann, A., Bottini, C., Brassell, S.C., Farnsworth, A., Forster, A., Huber, B.T., Inglis, G.N., Jenkyns, H.C., Linnert, C., Littler, K., Markwick, P., McAnena, A., Mutterlose, J., A. Naafs, B.D., Püttmann, W., Sluijs, A., van Helmond, N.A.G.M., Vellekoop, J., Wagner, T., Wrobel, N.E. 2017. Cretaceous sea-surface temperature evolution: Constraints from TEX86 and planktonic foraminiferal oxygen isotopes. Earth-Science Reviews, 172, 224-247.

Ovechkina, M. N., Erba, E., & Bottini, C. 2019. Calcareous nannoplankton proxies for palaeoenvironmental reconstruction of the Albian–Cenomanian succession in North-western Israel (Mount Carmel Region). Marine Micropaleontology. doi: 10.1016/j.marmicro.2019.04.001

Pattan, J.N., Pearce, N.J.G., Mislankar, P.G., 2005. Constraints in using Cerium-anomaly of bulk sediments as an indicator of paleo bottom water redox environment: A case study from the Central Indian Ocean Basin. Chemical Geology 221, 260–278.

Paytan, A., Griffith, E.M., 2007. Marine barite: Recorder of variations in ocean export productivity. Deep-Sea Res Pt II 54, 687–705.

Pedersen, T.F., Calvert, S.E., 1990. Anoxia vs. productivity: what controls the formation of organic-rich sediments and sedimentary rocks? AAPG Bull. 74, 454– 466.

Perkins, R.B., Piper, D.Z., Mason, C.E., 2008. Trace-element budgets in the Ohio/Sunbury shales of Kentucky: constraints on ocean circulation and primary productivity in the Devonian–Mississippian Appalachian Basin. Palaeogeography Palaeoclimatology Palaeoecology 265, 14–29.

Petrizzo, M.R., Huber, B.T., 2006. Biostratigraphy and taxonomy of late Albian planktonic foraminifera from ODP Leg 171B (western North Atlantic Ocean). Journal of Foraminiferal Research 36(2), 166–190.

Petrizzo, M.R., Huber, B.T., Wilson, P.A., MacLeod, K.G., 2008. Late Albian paleoceanography of the western subtropical North Atlantic. Paleoceanography 23(1), PA1213, https://doi.org/10.1029/2007PA001517.

Piper, D.Z., Calvert, S.E., 2009. A marine biogeochemical perspective on black shale deposition. Earth Science Reviews 95, 63–96.

Pratt, L.M., King, J.D., 1986. Variable marine productivity and high eolian input recorded by rhythmic black shales in Mid-Cretaceous pelagic deposits from central Italy, Paleoceanography 1, 507–522, doi: 10.1029/PA001i004p00507.

Reichelt, K., 2005. Late Aptian-Albian of the Vocontian Basin (SE-France) and Albian of NE-Texas: Biostratigraphic and paleoceanographic implications by planktic foraminifera faunas. Dissertation zur Erlangung des Grades eines Doktors der Naturwissenschaften, der Geowissenschaftlichen Fakultät der Eberhard-Karls-Universitat Tübingen, 125 pp.

Retallack, G.J., 2009. Greenhouse crises of the past 300 million years. Geological Society of America Bulletin 121(9-10), 1441–1455.

Richey, J.D., Upchurch, G.R., Montañez, I.P., Lomax, B.H., Suarez, M.B., Crout, N.M., Joeckel, R.M., Ludvigson, G.A., Smith, J.J., 2018. Changes in CO2 during Ocean Anoxic Event 1d indicate similarities to other carbon cycle perturbations. Earth and Planetary Science Letters 491, 172–182.

Robinson, S.A., Clarke, L.J., Nederbragt, A., Wood, I.G., 2008. Mid-Cretaceous oceanic anoxic events in the Pacific Ocean revealed by carbon-isotope stratigraphy of the Calera Limestone, California, USA. Geological Society of America Bulletin 120(11-12), 1416–1426.

Rodríguez-Cuicas, M.-E., Montero-Serrano, J.C., Garbán, G., 2019. Paleoenvironmental changes during the late Albian oceanic anoxic event 1d: An example from the Capacho Formation, southwestern Venezuela. Palaeogeography, Palaeoclimatology, Palaeoecology 521, 10–29.

Rodríguez-Cuicas, M.-E., Montero-Serrano, J.C., Garbán, G., 2020. Geochemical and mineralogical records of late Albian oceanic anoxic event 1d (OAE-1d) in the La Grita Member (southwestern Venezuela): Implications for weathering and provenance. Journal of South American Earth Sciences 97, 102408.

Rosenthal, Y., Lam, P., Boyle, E.A., Thomson, J., 1995. Authigenic cadmium enrichments in suboxic sediments: Precipitation and postdepositional mobility, Barth and Planetary Science Letters 132, 99–111.

Sageman, B.B., Lyons, T.W., 2005. Geochemistry of Fine-grained Sediments and Sedimentary Rocks, in: Holland, H.D., Turekian, K.K. (Eds.), Sediments, Diagenesis, and Sedimentary Rocks. Treatise on Geochemistry, vol. 7. Elsevier, Amsterdam, pp.115–158.

Scheiderich, K., Zerkle A.L., Helz, G.R., Farquhar, J., Walker, R.J., 2010. Molybdenum isotope, multiple sulfur isotope, and redox-sensitive element behavior in early Pleistocene Mediterranean sapropels. Chemical Geology 279, 134–144.

Schneider, R.R., Price, B., Müller, P.J., Kroon, D., Alexander, I., 1997. Monsoon related variations in Zaire (Congo) sediment load and influence of fluvial silicate supply to productivity in the east equatorial Atlantic during the last 200,000 years. Paleoceanography 12, 463–481.

Schnetger, B., 1992. Chemical composition of loess from a local and wordwide view. Neues Jahrbuch Mineralogische Abhandlungen, Monatshefte H. 1, 29–47.

Schnetger, B, Brumsack, H.-J., Schale, H., Hinrichs, J., Dittert, L., 2000. Geochemical characteristics of deep-sea sediments from the Arabian Sea: a high-resolution study. Deep Sea Research II 47, 2735–2768.

Schoepfer, S.D., Shen, J., Wei, H.Y., Tyson, R.V., Ingall, E., Algeo, T.J., 2015. TOC, organic P, and biogenic Ba accumulation rates as proxies for marine primary productivity and export flux. Earth-Science Reviews 149, 23–52.

Schwarzacher, W., 1994. Cyclostratigraphy of the Cenomanian in the Gubbio district, Italy: a field study, in: de Boer, P.L., Smith, D.G. (Eds.), Orbital forcing and cyclic sequences. Special Publication International Association of Sedimentologists Vol. 19, Gent, Belgium, pp. 99–107.

Scott, C., Lyons, T.W., 2012. Contrasting molybdenum cycling and isotopic properties in euxinic versus non-euxinic sediments and sedimentary rocks: Refining the paleoproxies. Chemical Geology 324–325, 19–27.

Scott, R.W., Formolo, M., Rush, N., Owens, J.D., Oboh-Ikuenobe, F., 2013. Upper Albian OAE 1d event in the Chihuahua Trough, New Mexico, USA. Cretaceous Research 46, 136–150.

Skelton, P.W., Spicer, R.A., Kelley, S.P., Gilmour I., 2003. The Cretaceous World, Cambridge Univ. Press, Cambridge, U.K..

Sprovieri, M., Sabatino, N., Pelosi, N., Batenburg, S.J., Coccioni, R., Iavarone, M., Mazzola, S., 2013. Late Cretaceous orbitally-paced carbon isotope stratigraphy from the Bottaccione Gorge (Italy). Palaeogeography, Palaeoclimatology, Palaeoecology 379, 81–94.

Stoll, H.M., Schrag, D.P., 2000. High-resolution stable isotope records from the Upper Cretaceous rocks of Italy and Spain: glacial episodes in a greenhouse planet? Geologica Society of America Bulletin 112, 308–319.

Strasser, A., Caron, M., Gjermeni, M., 2001. The Aptian, Albian and Cenomanian of Roter Sattel, Romandes Prealps, Switzerland: a high-resolution record of oceanographic changes. Cretaceous Research 22, 173–199.

Takashima, R., Kawabe, F., Nishi, H., Moriya, K., Wani, R., Ando, H., 2004. Geology and stratigraphy of forearc basin sediments in Hokkaido, Japan: Cretaceous environmental events on the north-west Pacific margin. Cretaceous Research 25(3), 365–390.

Taylor, S.R., McLennan, S., 1985. The Continental Crust: Its Composition and Evolution. Blackwell, Oxford, 312 p.

Tiraboschi, D., Erba, E., Jenkyns, H.C., 2009. Origin of rhythmic Albian black shales (Piobbico core, central Italy): Calcareous nannofossil quantitative and statistical analyses and paleoceanographic reconstructions. Paleoceanography 24, PA2222, doi: 10.1029/2008PA001670.

Torres, M.E., Brumsack, H.J., Bohrmann, G., Emeis, K.C., 1996. Barite fronts in continental margin sediments: a new look at barium remobilization in the zone of sulfate reduction and formation of heavy barites in diagenetic fronts. Chem. Geol. 127, 125– 139.

Tribovillard, N., Algeo, T.J., Lyons, T., Riboulleau, A., 2006. Trace metals as paleoredox and paleoproductivity proxies: an update. Chemical Geology 232, 12–32.

Tsikos, H., Jenkyns, H.C., Walsworth-Bell, B., Petrizzo, M.R., Forster, A., Kolonic, S., Erba, E., Premoli Silva, I., Baas, M.,Wagner, T., Sinninghe Damsté, J.S., 2004. Carbon-isotope stratigraphy recorded by the Cenomanian–Turonian Oceanic Anoxic Event: correlation and implications based on three key localities. Journal of the Geologiacal Society of London 161, 711–719.

Turgeon, S., Brumsack, H.-J., 2006. Anoxic vs dysoxic events reflected in sediment geochemistry during the Cenomanian–Turonian Boundary Event (Cretaceous) in the Umbria–Marche Basin of central Italy. Chemical Geology 234, 321–339.

Tyson, R.V., 1995. Sedimentary Organic Matter. Organic Facies and Palynofacies, Chapman and Hall, London, 615 pp.

Tyson, R.V., 2005. The “productivity versus preservation” controversy; cause, flaws, and resolution, in: Harris, N.B. (Ed.), Deposition of Organic-Carbon-Rich Sediments: Models Mechanisms, and Consequences. SEPM Special Publication 82, Tulsa, OK, pp. 17–33.

Vahrenkamp, V.C., 2013. Carbon isotope signatures of Albian to Cenomanian (Cretaceous) shelf carbonates of the Natih Formation, Sultanate of Oman. GeoArabia 18, 65–82.

Wang, X., Lang, L., Hua, T., Zhang, C., Li, H., 2017. The effects of sorting by aeolian processes on the geochemical characteristics of surface materials: a wind tunnel experiment. Frontiers of Earth Science 12(1), 86–94.

Watkins, D.K., Cooper, M.J., Wilson, P.A., 2005. Calcareous nannoplankton response to late Albian oceanic anoxic event 1d in the western North Atlantic. Paleoceanography and Paleoclimatology 20(2), PA2010, doi:10.1029/2004PA001097.

Wedepohl, K.H., 1971. Environmental influences on the chemical composition of shales and clays. In: Ahrens, L.H., Press, F., Runcorn, S.K., Urey, H.C. (Eds.), Physics and Chemistry of the Earth, vol. 8. Pergamon, Oxford, pp. 305–333.

Wedepohl, K.H., 1991. The composition of the upper earth's crust and the natural cycles of selected metals. Metals in natural raw materials. Natural resources. In: Merian, E. (Ed.), Metals and their Compounds in the Environment. VCH, Weinheim, pp. 3–17.

Wilson, P.A., Norris, R.D., 2001. Warm tropical ocean surface and global anoxia during the mid-Cretaceous period. Nature 412, 425–429.

Wohlwend, S., Hart, M.B., Weissert, H., 2016. Chemostratigraphy of the Upper Albian to mid-Turonian Natih Formation (Oman) – or: how authigenic carbonate changes a global pattern. The Depositional Record 2, 97–117.

Yao, H., Chen, X., Melinte-Dobrinescu, M.C., Wu, H., Liang, H., Weissert, H., 2018. Biostratigraphy, carbon isotopes and cyclostratigraphy of the Albian-Cenomanian transition and Oceanic Anoxic Event 1d in southern Tibet. Palaeogeography, Palaeoclimatology, Palaeoecology 499, 45–55.

Zaid, S.M., El-Badry, O.A., Akarish, A.M., Mohamed, M.A., Provenance, weathering, and paleoenvironment of the Upper Cretaceous Duwi black shales, Aswan Governorate, Egypt. Arabian Journal of Geosciences 11: 147, doi: 10.1007/s12517-018-3500-z.

Zhang, X., Chen, K., Hu, D., Sha, J., 2016. Mid-Cretaceous carbon cycle perturbations and Oceanic Anoxic Events recorded in southern Tibet. Scientific reports, 6, 39643, doi: 10.1038/srep39643.

Zonneveld, K.A.F., Versteegh, G.J.M., Kasten, S., Eglinton, T.I., Emeis, K.C., Huguet, C., Koch, B.P., de Lange, G.J., Middelburg, J.J., Mollenhauer, G., Prahl, F.G., Rethemeyer, J., Wakeham, S.G., 2010. Selective preservation of organic matter in marine environments; processes and impact on the sedimentary record. Biogeosciences 7, 483–511.

Figure captions

Figure 1: A. Map of Italy with the position of the Umbria-Marche Basin; B. Schematic map reporting the position of the Monte Petrano and Le Brecce sections; C. Paleogeographic reconstruction of the western Tethys during the late Albian-early Cenomanian (c.a.100 Ma) (modified after https://deeptimemaps.com/europe-series/). Red star shows the relative paleo-position of the Umbria-Marche Basin; D. Schematic bio- and chemo-stratigraphy of the late Albian OAE 1d carbon isotope excursion (smoothed isotopic data and biostratigraphy from the Monte Petrano section (after Gambacorta et al., 2015; Gilardoni, 2017).

Figure 2: A. Panoramic view of the Monte Petrano section. The white bar indicates the studied interval (0 to 35 m); B. Basal part of the Scaglia Bianca Formation at Le Brecce section (from about 2 to 4.5 m). Hammer for scale; C. Black shale layer at about 11.6 m (MP 3) at Monte Petrano section. The black shale is about 6 cm thick; D. Black shale layer at about 10.0 m (BR 5) at Le Brecce section. The black shale is about 4 cm thick and is overlaid by about 5 cm of light brown marls.

Figure 3: Litho-, bio- and chemostratigraphic correlation of the Monte Petrano and Le Brecce sections. Chemo- and biostratigraphic data from Gambacorta et al. (2015) and Gilardoni, (2017). The stratigraphic extent of the OAE 1d and the relative position of the Pialli Level black-to-dark grey shale layers (MP – Monte Petrano, BR – Le Brecce) are reported. See text for details. The Albian/Cenomanian boundary is placed at the FO of *Th. globotruncanoides* (Gilardoni, 2017).

Table 1a: Average major and trace elements measured values of analyzed limestones from the Monte Petrano section. All oxides are reported as %, minor and trace elements in µg/g.

All trace element/Al and Mn/Al ratios are expressed as $\times 10^{-4}$. Average elements and element/Al standard deviations (1 σ), maximum values and enrichment factors (EF) are shown. Average shale (AS) values from Wedepohl (1971, 1991).

Table 1b: Average major and trace elements measured values of analyzed black-to-dark grey shales from the Monte Petrano section. All oxides are reported as %, minor and trace elements in µg/g, except for Re (ng/g). All trace element/Al and Mn/Al ratios are expressed as $\times 10^{-4}$, except for Re ($\times 10^{-7}$). Average elements and element/Al standard deviations (1 σ), maximum values and enrichment factors (EF) are shown. Average shale (AS) values from Wedepohl (1971, 1991), except Re from Crusius et al. (1996).

Table 2a: Average major and trace elements measured values of analyzed limestones from Le Brecce section. All oxides are reported as %, minor and trace elements in µg/g. All trace element/Al and Mn/Al ratios are expressed as $\times 10^{-4}$. Average elements and element/Al standard deviations (1 σ), maximum values and enrichment factors (EF) are shown. Average shale (AS) values from Wedepohl (1971, 1991).

Table 2b: Average major and trace elements measured values of analyzed black-to-dark grey shales from Le Brecce section. All oxides are reported as %, minor and trace elements in µg/g, except for Re (ng/g). All trace element/Al and Mn/Al ratios are expressed as $\times 10^{-4}$, except for Re ($\times 10^{-7}$). Average elements and element/Al standard deviations (1 σ), maximum values and enrichment factors (EF) are shown. Average shale (AS) values from Wedepohl (1971, 1991), except Re from Crusius et al. (1996).

Figure 4: Enrichment factors (relative to average shale of Wedepohl, 1971, 1991, except Re from Crusius et al., 1996) of analyzed black-to-dark grey shales from Monte Petrano and Le Brecce sections.

Figure 5: Comparison of average REE pattern normalized to Average Post-Archaean Australian Shale (PAAS) (Taylor and McLennan, 1985) between the black-to-dark grey shales of the Monte Petrano section (filled red triangles) and the dark grey shales of Le Brecce section (filled blue circles).

Figure 6: Panel reporting data from the Monte Petrano section. From left to right: nannofossil and planktonic foraminifera biostratigraphy (from Gambacorta et al., 2015 and Gilardoni, 2017); schematic lithological column; total organic carbon (TOC) and TOC/Al ratio; carbon and oxygen isotopic data (from Gambacorta et al., 2015); nannofossil temperature (TI) and nutrient (NI) indices; the relative abundance (%) of the warm-water species *R. asper* is reported on the left side of the TI (red part of the curve) for all samples with TI=0 and it highlights the temperature fluctuations within the warm climatic regime; the reference line at NI=35 corresponds to the average NI of the sections and it is here adopted to divide samples of lower fertility from those of higher fertility; productivity (P/Al, Ba_{xs}, Ni/Al, Cd/Al) and redox-sensitive (Mn/Al, V/Al, Co/Al, U/Al) trace element stratigraphic distribution. The vertical line in the P/Al, Ni/Al, Cd/Al, Mn/Al, V/Al, Co/Al, U/Al graphs represents average shale (AS) composition according to Wedepohl (1971, 1991). For the sake of readability, the P/Al and Co/Al axes are cropped and the Cd/Al axis is in logarithmic scale. Data relative to the limestone and black-to-dark grey shale samples are reported with black and red dots respectively. Background shading indicates the intervals interpreted as characterized by warmer (light red) and relatively cooler (light blue) climatic conditions. The position of the OAE1d is indicated by a white bar. Cooler and warmer intervals 1 to 4 reported on the right

side of the panel are defined and described in the text. For lithological keys see legend in Figure 3.

Figure 7: Panel reporting data from Le Brecce section. From left to right: nannofossil and planktonic foraminifera biostragraphy (from Gambacorta et al., 2015 and Gilardoni, 2017); schematic lithological column; total organic carbon (TOC) and TOC/Al ratio; carbon and oxygen isotopic data (from Gambacorta et al., 2015); nannofossil temperature (TI) and nutrient (NI) indices; the relative abundance (%) of the warm-water species *R. asper* is reported on the left side of the TI (red part of the curve) for all samples with TI=0 and it highlights the temperature fluctuations within the warm climatic regime; the reference line at NI=35 corresponds to the average NI of the sections and it is here adopted to divide samples of lower fertility from those of higher fertility; productivity (P/Al, Ba_{xs}, Ni/Al, Cd/Al) and redox-sensitive (Mn/Al, V/Al, Co/Al, U/Al) trace element stratigraphic distribution. The vertical line in the P/Al, Ni/Al, Cd/Al, Mn/Al, V/Al, Co/Al, U/Al graphs represents average shale (AS) composition according to Wedepohl (1971, 1991). For the sake of readability, the Ba_{xs} and Co/Al axes are cropped and the Cd/Al axis is in logarithmic scale. Data relative to the limestone and black-to-dark grey shale samples are reported with black and red dots respectively. Background shading indicates the intervals interpreted as characterized by warmer (light red) and relatively cooler (light blue) climatic conditions. The position of the OAE 1d is indicated by a white bar. Cooler and warmer intervals 1 to 3 reported on the right side of the panel are defined and described in the text. For lithological keys see legend in Figure 3.

Figure 8: Ternary diagram of relative proportions of Al_2O_3 (×5), SiO_2, and CaO for samples from the Monte Petrano (limestones open red triangles, black-to-dark grey shales filled red triangles) and Le Brecce (limestones open blue circles, black-to-dark grey shales filled blue

circles) sections. Monte Petrano and Le Brecce black-to-dark-grey shale samples are indicated with MP and BR respectively following the code used in Figure 3. For Al_2O_3 an arbitrary multiplier of 5 is used in order to better distribute the data points in the graph. The average shale (AS) composition (Wedepohl, 1971, 1991) and the carbonate dilution line (red line) are reported. See text for details.

Figure 9: Cross-plots of lithogenic conservative elements (SiO_2, TiO_2, K_2O, Fe_2O_3, Rb, Zr) versus Al_2O_3 for samples from the Monte Petrano (limestones open red triangles, black-to-dark grey shales filled red triangles) and Le Brecce (limestones open blue circles, black-to-dark grey shales filled blue circles) sections. Monte Petrano and Le Brecce black-to-dark-grey shale samples are indicated with MP and BR respectively following the code used in Figure 3. The average shale (AS) line, that connects the origin of the graph to the average shale composition, is reported in each plot.

Figure 10: Cross-plot of carbonate carbon- and oxygen-isotope ratios for samples analysed from the Monte Petrano (open red triangles) and Le Brecce (open blue circles).

Table 3: Average enrichment factors and deviation standards of major redox-sensitive elements/Al and TOC for studied dark grey shales (MP1, MP2, MP6; BR1, BR2, BR6) interpreted as deposited under oxic to feeble reducing settings and analyzed black shales (MP3, MP4, MP5; BR3, BR4, BR5) associated with suboxic conditions.

Figure 11: Re vs Mo diagram for Monte Petrano (filled red triangles) and Le Brecce (filled blue circles) black-to-dark-grey shale samples. The red square represents average shale (AS) composition (Wedepohl, 1971, 1991). The seawater Re/Mo value (~0.8) is reported

together with the Re/Mo ~10 cutoff value for suboxic versus anoxic sediments (Scheiderich et al., 2010). See text for details.

Table 4: Local background values for Si/Al and Ba/Al. Ba/Al ratios are expressed as $\times 10^{-4}$.

Figure 12: Surface water fertility and temperature conditions reconstructed on the basis of calcareous nannofossils, and occurrence of oxygen depletion within the sediments at Monte Petrano (this study), Col de Palluel (Bornemann et al., 2005), Blieux section (Giraud et al., 2003), Anderten 1 and 2 cores (Bornemann et al., 2017), and ODP Site 1052 (Watkins et al., 2005). Redox conditions are estimated at Monte Petrano (this study) and on the Anderten 1 and 2 cores (Bornemann et al., 2017) based on elemental data, while palaeo-oxygenation for the Blieux section is based on the ichnoassemblages and on the intensity and maximum diameter of the burrows (Giraud et al., 2003). NI = Nutrient Index based on nannofossils. TI = Temperature Index based on nannofossils. The dark grey band highlights the OAE 1d. Black shale distribution, planktonic and nannofossil biostratigraphy and carbon isotope profiles for the OAE 1d interval are reported for each section: Monte Petrano (Gambacorta et al., 2015), Col de Palluel (Bornemann et al., 2005), Anderten 1 and 2 cores (Bornemann et al., 2017), and ODP Site 1052 (Wilson and Norris, 2001).

Figure 13: Schematic depositional model (not to scale) representing the major chemical processes involved during the deposition of the Pialli Level black-to-dark grey shales. See text for details.

Supplementary material captions

Table A: Major and trace element content and nannofossil indices data for the analyzed samples from the Monte Petrano section.

Table B: Major and trace element content and nannofossil indices data for the analyzed samples from Le Brecce section.

Figure C: Stratigraphic distribution of lithogenic conservative elements (Si, Ti, K, Fe, Rb, Zr) versus Al at the Monte Petrano section. For the sake of readability, the Si/Al axis is cropped. Black-to-dark grey shale samples are indicated with MP following the code used in Figure 3. The vertical line in the graphs represents average shale (AS) composition according to Wedepohl (1971, 1991).

Figure D: Stratigraphic distribution of lithogenic conservative elements (Si, Ti, K, Fe, Rb, Zr) versus Al at Le Brecce section. For the sake of readability, the Si/Al axis is cropped. Black-to-dark grey shale samples are indicated with BR following the code used in Figure 3. The vertical line in the graphs represents average shale (AS) composition according to Wedepohl (1971, 1991).

Figure E: Crossplots reporting Al-normalized redox-sensitive element composition with weak- (Cu, Ni, Cr, Co) and strong- (Mo, U, V, Zn, Pb) euxinic affinity versus TOC for the black-to-dark grey shale layers at Monte Petrano and Le Brecce sections. Redox thresholds follow Algeo and Maynard (2004).

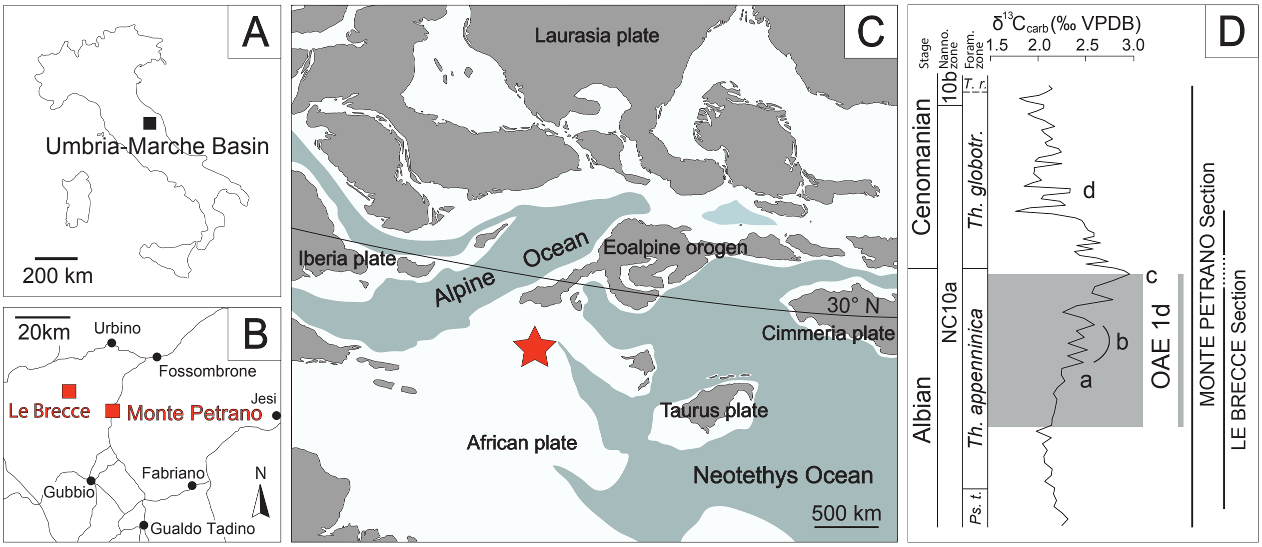
A
Umbria-Marche Basin
200 km
B
20km
Urbino
Fossombrone
Jesi
Le Brecce
Monte Petrano
Gubbio
Fabriano
N
Gualdo Tadino
C
Laurasia plate
Iberia plate
Alpine Ocean
Eoalpine orogen
30° N
Cimmeria plate
Taurus plate
African plate
Neotethys Ocean
500 km
D
Stage
Nanno. zone
Foram. zone
δ13Ccarb (‰ VPDB)
1.5 2.0 2.5 3.0
Cenomanian
Albian
10b
NC10a
T. r.
Th. globotr.
Th. appenninica
Ps. t.
a
b
c
d
OAE 1d
MONTE PETRANO Section
LE BRECCE Section

Figure 1

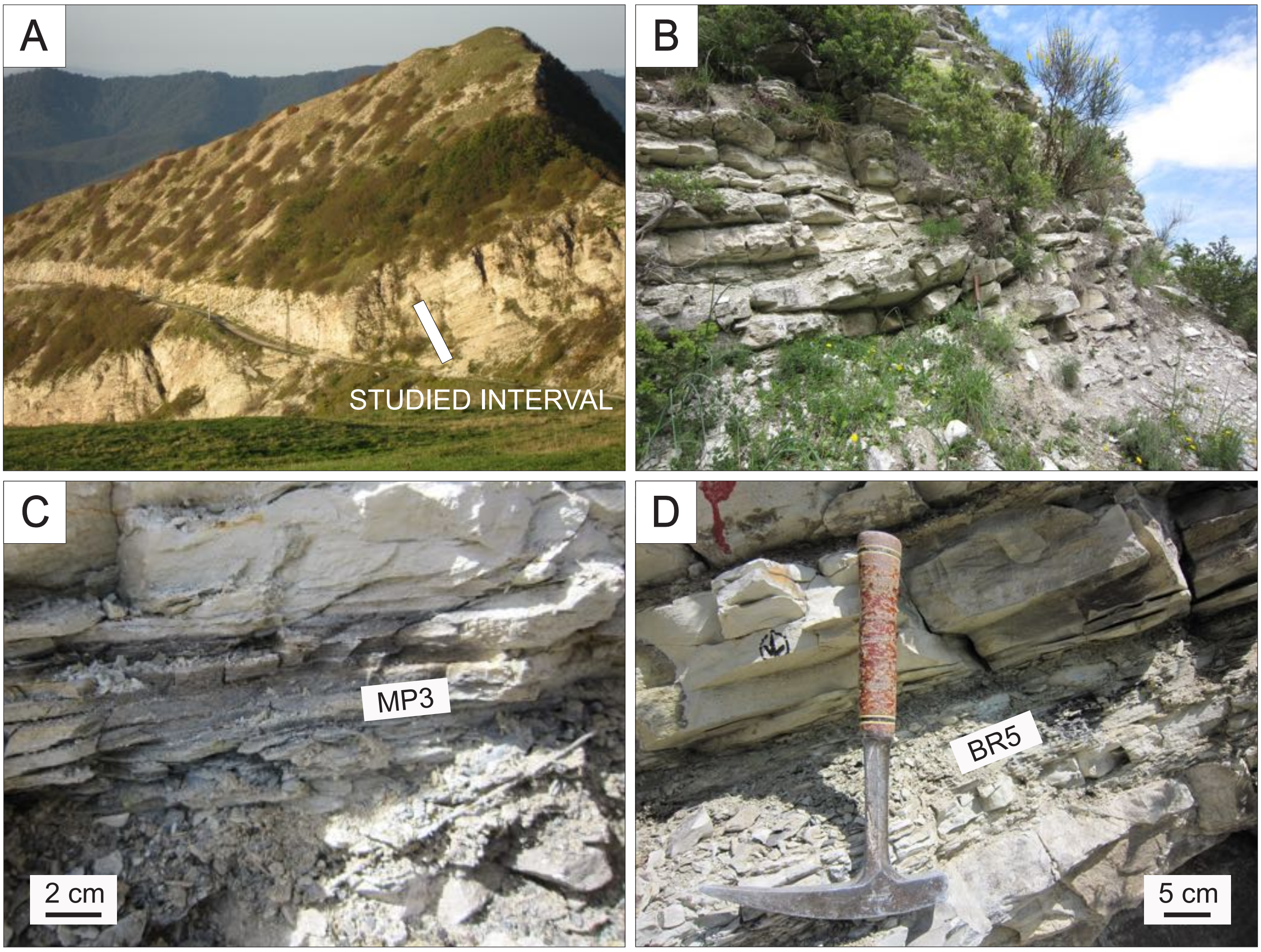

Figure 2

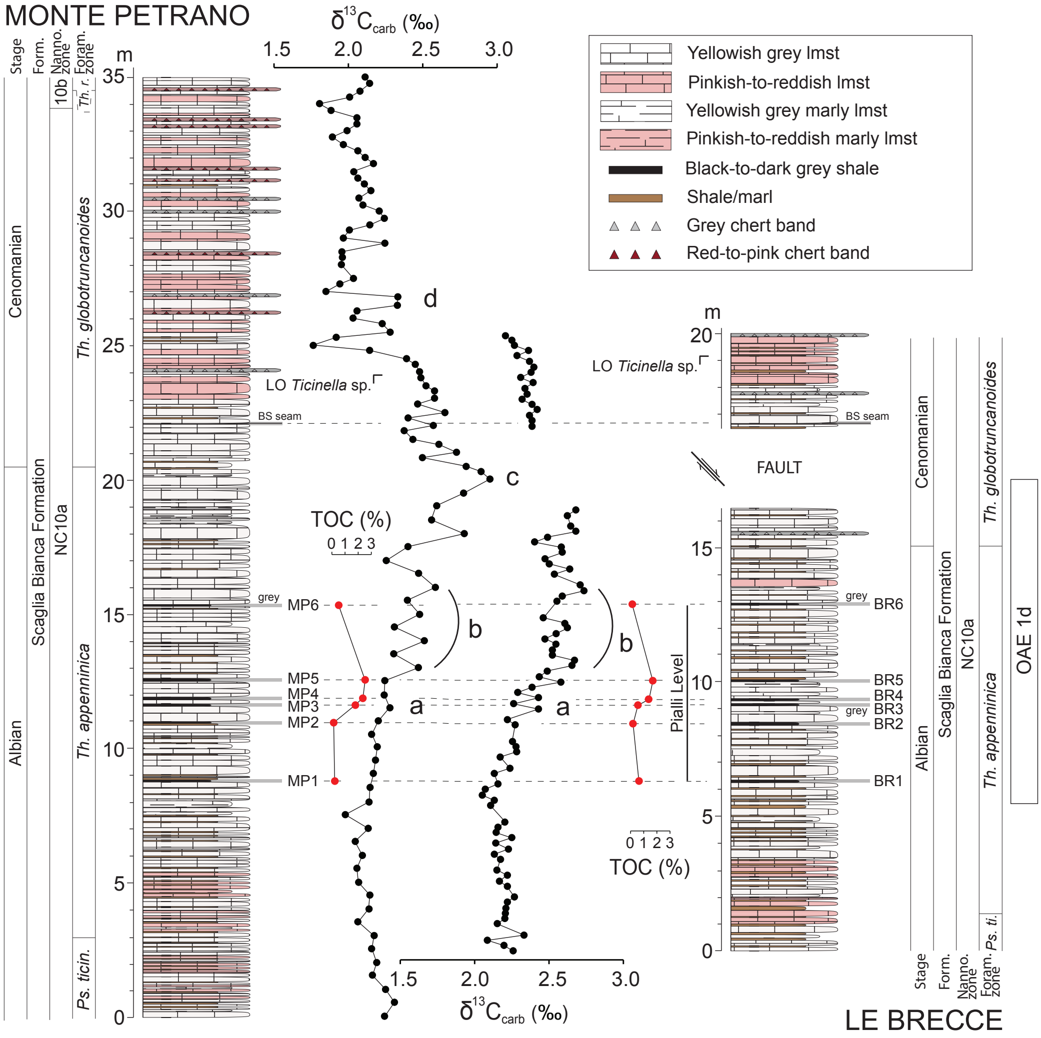

MONTE PETRANO
δ13Ccarb (‰)
1.5
2.0
2.5
3.0
Stage
Form.
Nanno. zone
Foram. zone
m
35
30
25
20
15
10
5
0
Cenomanian
Albian
Scaglia Bianca Formation
10b
NC10a
Th. r.
Th. globotruncanoides
Th. appenninica
Ps. ticin.
LO Ticinella sp.
BS seam
TOC (%)
0 1 2 3
grey
MP6
MP5
MP4
MP3
MP2
MP1
a
b
c
d
Yellowish grey lmst
Pinkish-to-reddish lmst
Yellowish grey marly lmst
Pinkish-to-reddish marly lmst
Black-to-dark grey shale
Shale/marl
Grey chert band
Red-to-pink chert band
FAULT
Pialli Level
BR6
BR5
BR4
BR3
BR2
BR1
Ps. ti.
OAE 1d
LE BRECCE

Figure 3

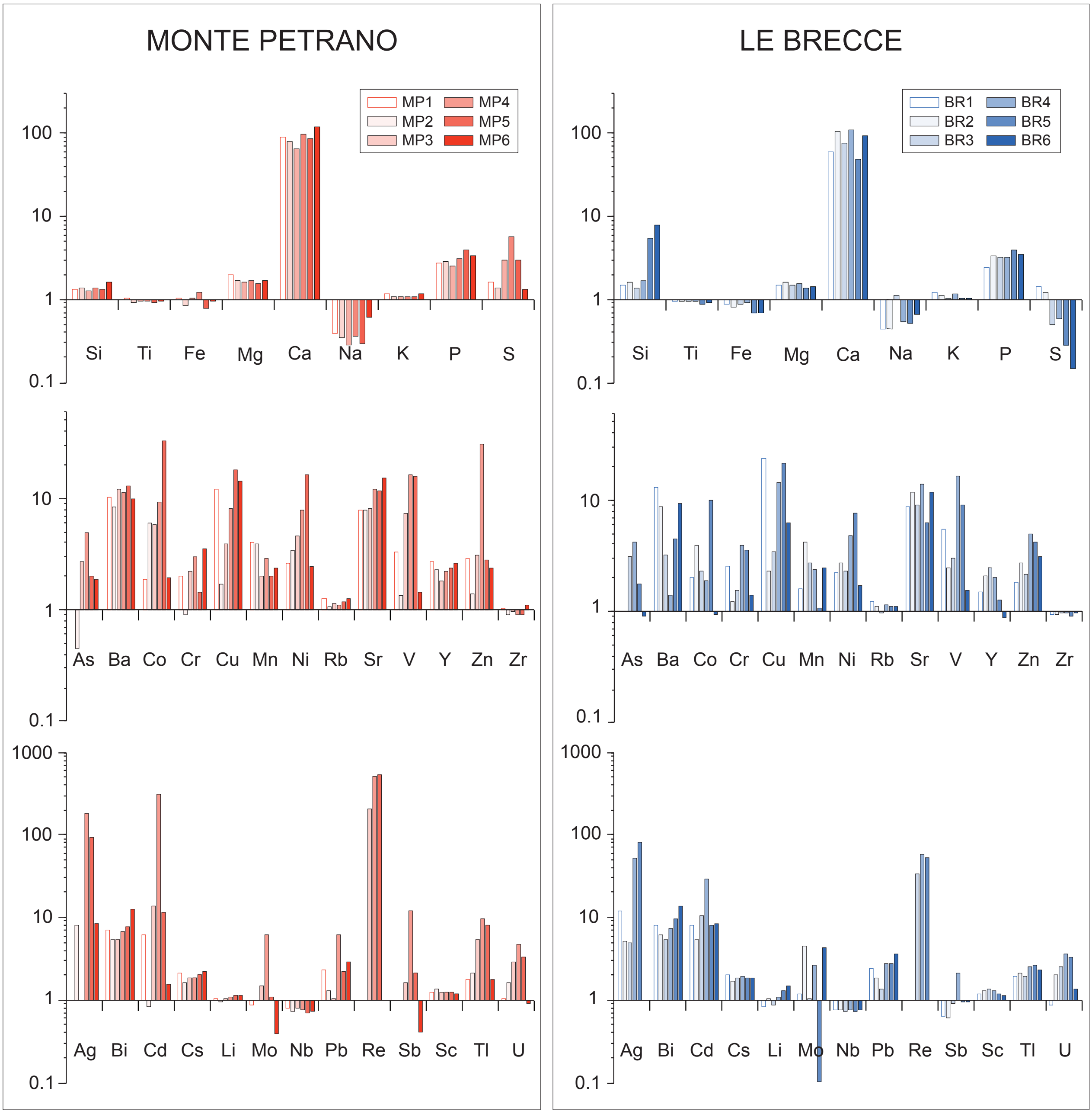

1358

1359 Figure 4

1360

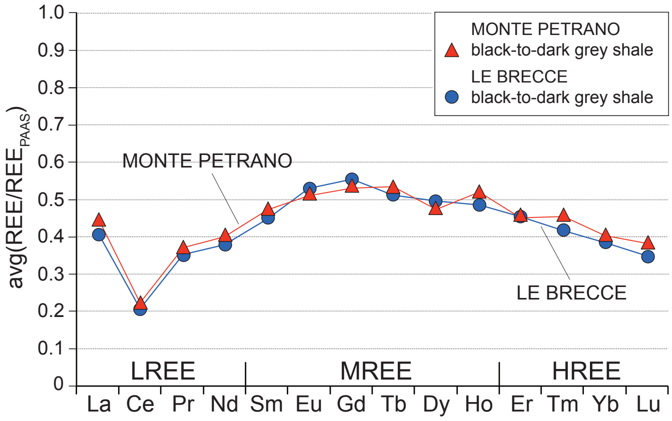

MONTE PETRANO
black-to-dark grey shale
LE BRECCE
black-to-dark grey shale
MONTE PETRANO
LE BRECCE
avg(REE/REE$_{PAAS}$)
1.0
0.9
0.8
0.7
0.6
0.5
0.4
0.3
0.2
0.1
0
LREE
MREE
HREE
La
Ce
Pr
Nd
Sm
Eu
Gd
Tb
Dy
Ho
Er
Tm
Yb
Lu

Figure 5

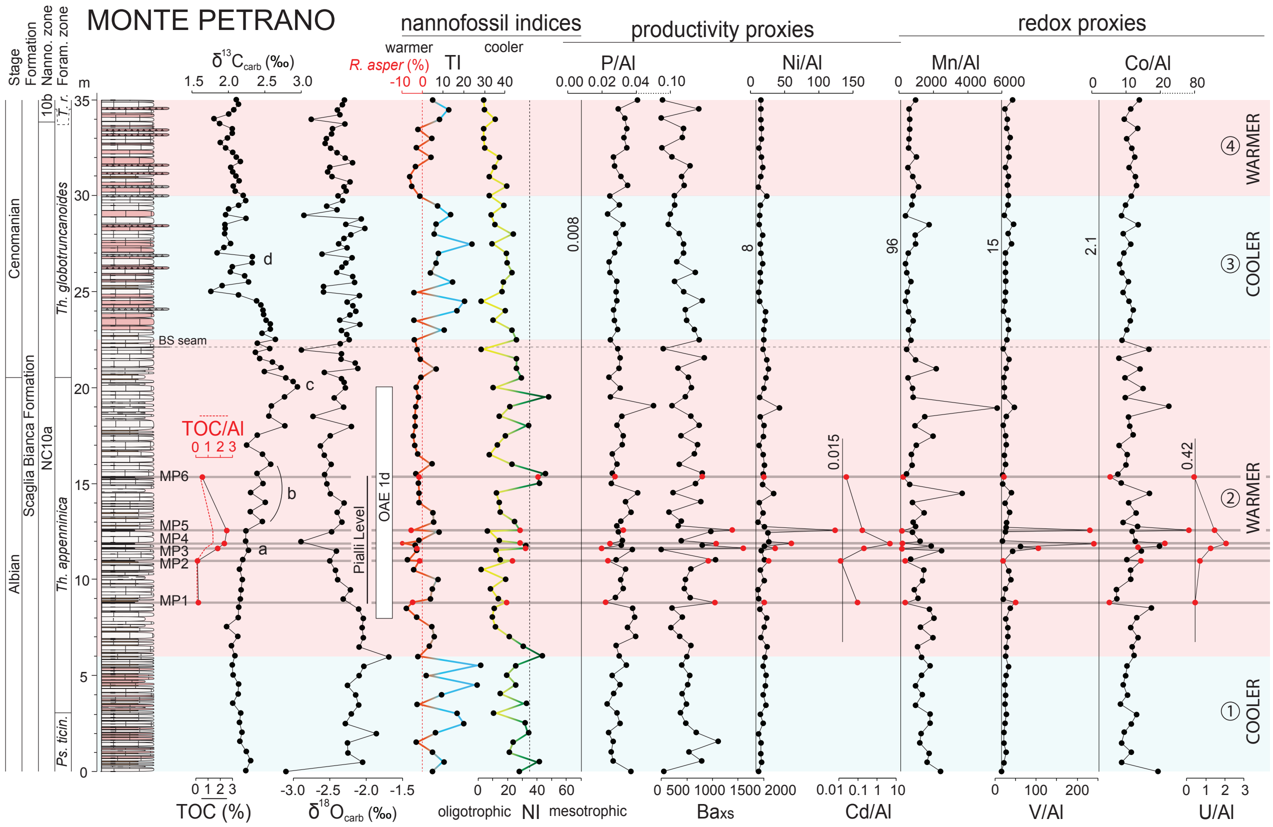

MONTE PETRANO
nannofossil indices
productivity proxies
redox proxies
Stage
Formation
Nanno. zone
Foram. zone
Cenomanian
Albian
Scaglia Bianca Formation
NC10a
10b
Th. globotruncanoides
Th. appenninica
Ps. ticin.
BS seam
TOC/Al
MP6
MP5
MP4
MP3
MP2
MP1
Pialli Level
OAE 1d
TOC (%)
warmer
cooler
R. asper (%)
TI
oligotrophic
NI
mesotrophic
P/Al
Ni/Al
Mn/Al
Co/Al
Baxs
Cd/Al
V/Al
U/Al
① COOLER
② WARMER
③ COOLER
④ WARMER

Figure 6

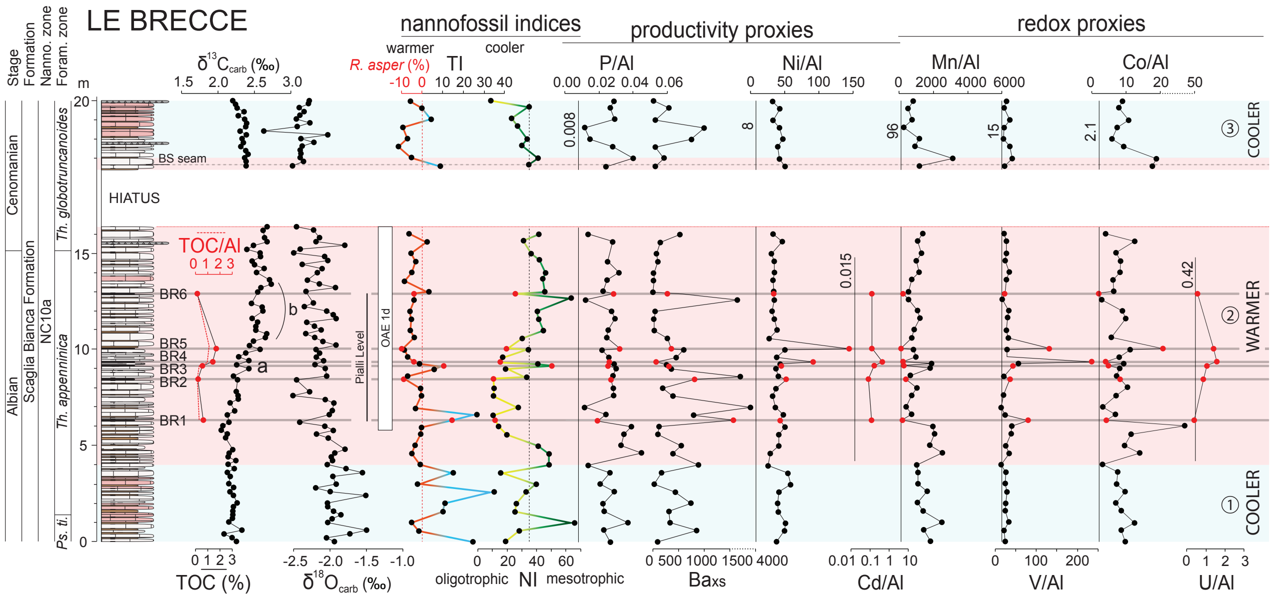

LE BRECCE
Stage
Formation
Nanno. zone
Foram. zone
m
Albian
Cenomanian
Scaglia Bianca Formation
NC10a
Th. appenninica
Th. globotruncanoides
Ps. ti.
HIATUS
BS seam
BR1
BR2
BR3
BR4
BR5
BR6
TOC/Al
Pialli Level
OAE 1d
nannofossil indices
productivity proxies
redox proxies
warmer
cooler
R. asper (%)
TI
P/Al
Ni/Al
Mn/Al
Co/Al
TOC (%)
oligotrophic
NI
mesotrophic
Baxs
Cd/Al
V/Al
U/Al
COOLER
WARMER

Figure 7

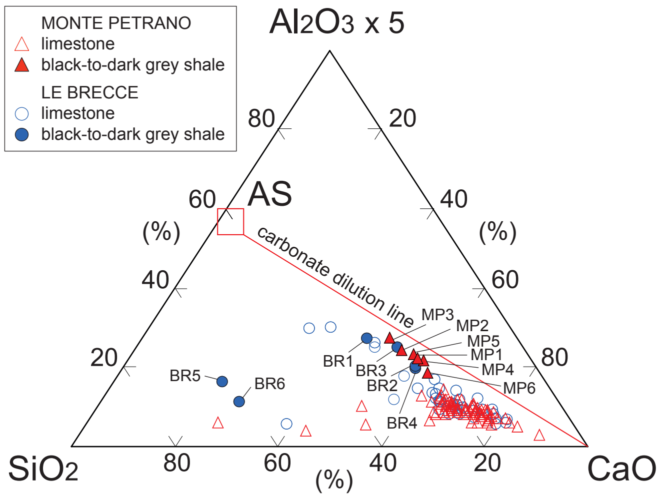
MONTE PETRANO
limestone
black-to-dark grey shale
LE BRECCE
limestone
black-to-dark grey shale
Al_2O_3 x 5
AS
carbonate dilution line
SiO_2
CaO
(%)
(%)
(%)
20
40
60
80
20
40
60
80
80
60
40
20
MP3
MP2
MP5
MP1
MP4
MP6
BR1
BR2
BR3
BR4
BR5
BR6

Figure 8

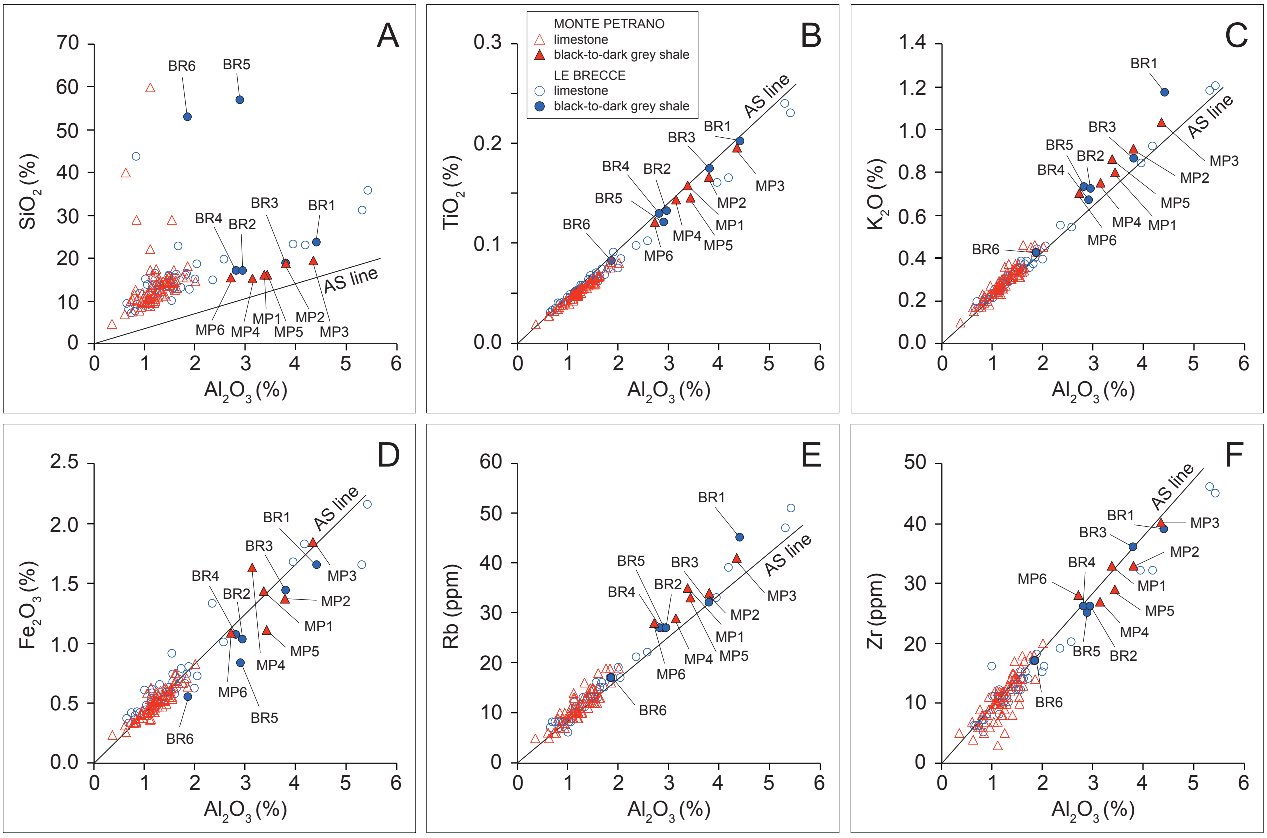
A
B
C
D
E
F
MONTE PETRANO
limestone
black-to-dark grey shale
LE BRECCE
limestone
black-to-dark grey shale
SiO2 (%)
TiO2 (%)
K2O (%)
Fe2O3 (%)
Rb (ppm)
Zr (ppm)
Al2O3 (%)
AS line
BR1
BR2
BR3
BR4
BR5
BR6
MP1
MP2
MP3
MP4
MP5
MP6

Figure 9

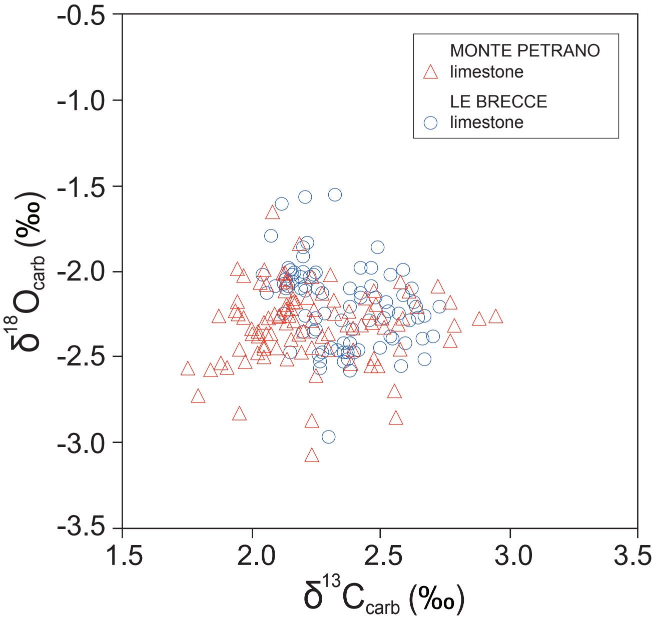
MONTE PETRANO
limestone
LE BRECCE
limestone
-0.5
-1.0
-1.5
-2.0
-2.5
-3.0
-3.5
1.5
2.0
2.5
3.0
3.5
δ18Ocarb (‰)
δ13Ccarb (‰)

Figure 10

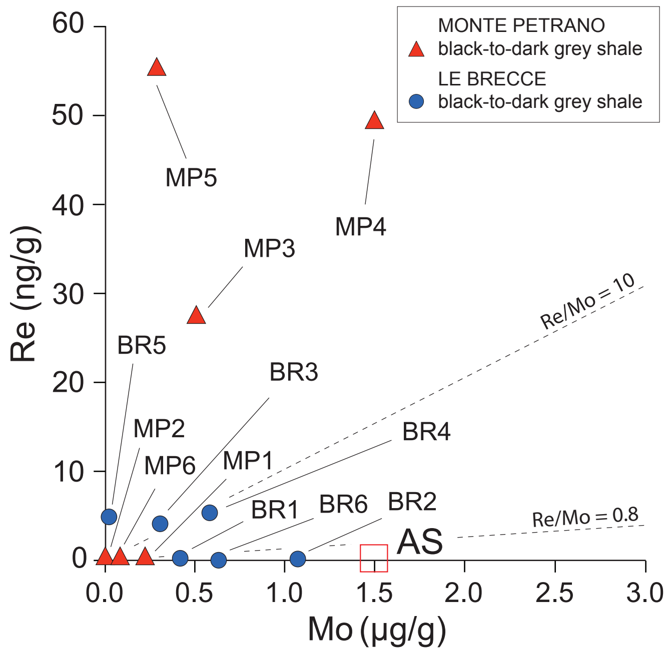
MONTE PETRANO
black-to-dark grey shale
LE BRECCE
black-to-dark grey shale
MP5
MP4
MP3
BR5
BR3
MP2
MP6
MP1
BR4
BR1
BR6
BR2
AS
Re/Mo = 10
Re/Mo = 0.8
Re (ng/g)
Mo (µg/g)
0
10
20
30
40
50
60
0.0
0.5
1.0
1.5
2.0
2.5
3.0

Figure 11

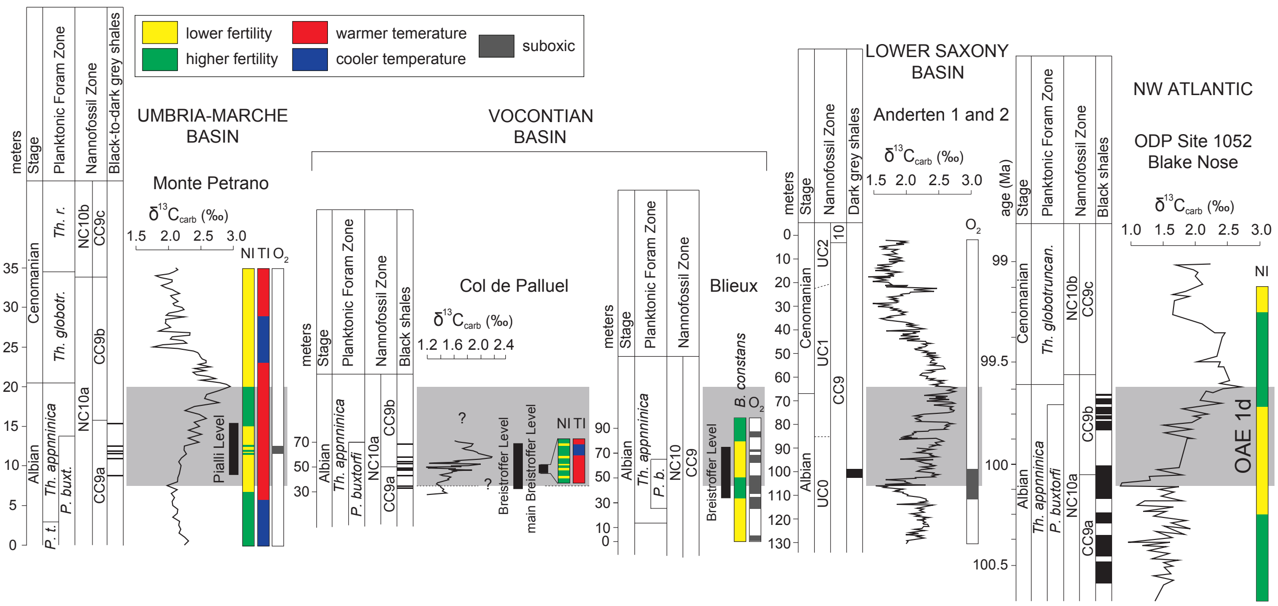
lower fertility
higher fertility
warmer temerature
cooler temperature
suboxic
UMBRIA-MARCHE BASIN
Monte Petrano
VOCONTIAN BASIN
Col de Palluel
Blieux
LOWER SAXONY BASIN
Anderten 1 and 2
NW ATLANTIC
ODP Site 1052 Blake Nose
meters
Stage
Planktonic Foram Zone
Nannofossil Zone
Black-to-dark grey shales
Black shales
Dark grey shales
age (Ma)
Cenomanian
Albian
Th. appnninica
P. buxtorfi
Th. globotruncan.
Pialli Level
Breistroffer Level
main Breistroffer Level
B. constans
NI
TI
O2
OAE 1d

Figure 12

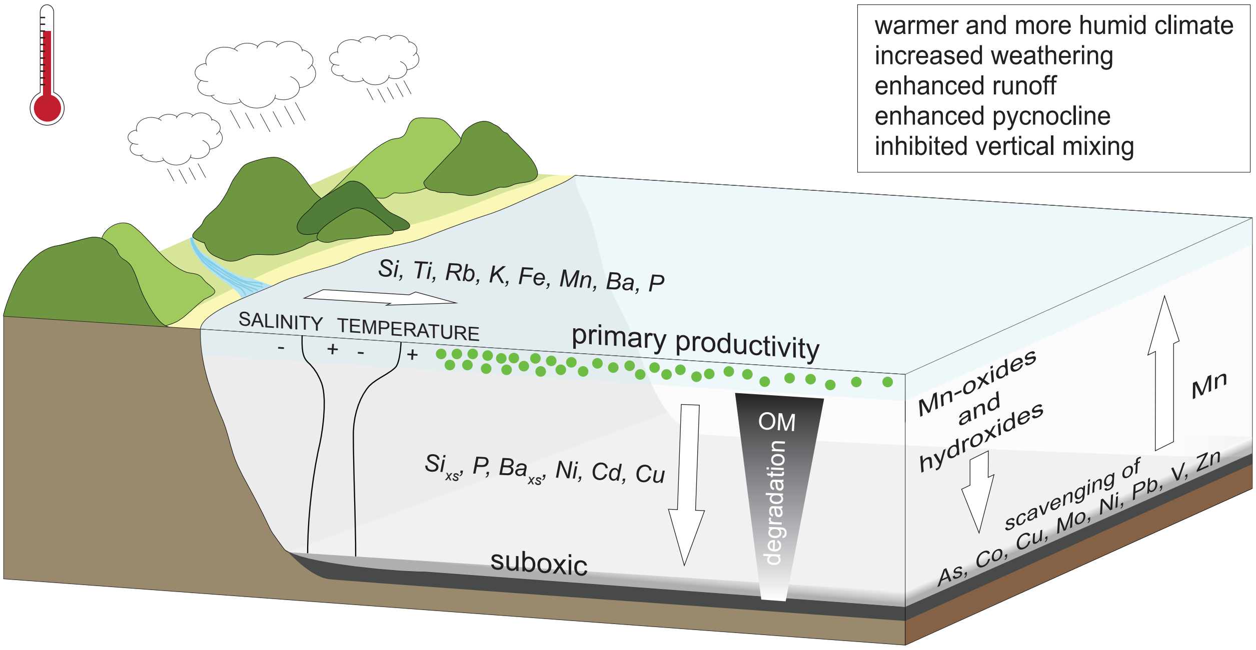
warmer and more humid climate
increased weathering
enhanced runoff
enhanced pycnocline
inhibited vertical mixing
Si, Ti, Rb, K, Fe, Mn, Ba, P
SALINITY
TEMPERATURE
- + - +
primary productivity
Mn-oxides and hydroxides
Mn
OM
degradation
Si_{xs}, P, Ba_{xs}, Ni, Cd, Cu
scavenging of As, Co, Cu, Mo, Ni, Pb, V, Zn
suboxic

Figure 13

Limestones (n= 73)									MONTE PETRANO
Element	conc	sigma	max	Average Shale	Element/Al	ratio	sigma	Average Shale	EF
SiO_2	14.1	7.4	59.7	58.9	Si/Al	10.80	7.68	3.11	3.5
TiO_2	0.05	0.05	0.08	0.78	Ti/Al	0.048	0.002	0.053	0.9
Al_2O_3	1.2	1.2	2.0	16.7	-	-	-	-	1.0
Fe_2O_3	0.5	0.5	0.8	6.9	Fe/Al	0.55	0.07	0.55	1.0
MgO	0.5	0.5	0.7	2.6	Mg/Al	0.47	0.14	0.18	2.7
CaO	46.5	46.5	53.0	2.2	Ca/Al	56.18	23.09	0.18	315.8
Na_2O	0.1	0.10	0.19	1.6	Na/Al	0.12	0.06	0.13	0.9
K_2O	0.3	0.3	0.5	3.6	K/Al	0.37	0.03	0.34	1.1
P_2O_5	0.04	0.04	0.06	0.16	P/Al	0.030	0.006	0.008	3.9
SO_3	0.06	0.06	0.18	0.60	S/Al	0.040	0.017	0.027	1.5
As	1	1	4	10	As/Al	1.6	2.0	1.1	1.4
Ba	511	511	1164	580	Ba/Al	782	325	66	11.9
Co	6	1	11	19	Co/Al	10.2	2.9	2.1	4.7
Cr	11	6	33	90	Cr/Al	17	10	10	1.7
Cu	12	9	44	45	Cu/Al	17.3	14.2	5.1	3.7
MnO	0.09	0.03	0.17	0.11	Mn/Al	1164	800	96	12.1
Ni	11	4	24	68	Ni/Al	17.8	5.3	7.7	2.3
Rb	11	3	19	140	Rb/Al	17	3	16	1.1
Sr	474	101	625	300	Sr/Al	774	246	34	22.8
V	18	4	36	130	V/Al	28	8	15	1.9
Y	11	3	17	41	Y/Al	17.4	4.6	4.6	3.8
Zn	16	4	33	95	Zn/Al	27	9	11	2.5
Zr	11	4	20	160	Zr/Al	17	3	18	0.9

Table 1a

Black-to-dark grey shales (n= 6)									**MONTE PETRANO**
Element	conc	sigma	max	Average Shale	Element/Al	ratio	sigma	Average Shale	EF
SiO_2	16.8	1.8	19.4	58.9	Si/Al	4.34	0.37	3.11	1.4
TiO_2	0.16	0.03	0.20	0.78	Ti/Al	0.051	0.002	0.053	1.0
Al_2O_3	3.5	0.6	4.3	16.7	-	-	-	-	1.0
Fe_2O_3	1.4	0.3	1.8	6.9	Fe/Al	0.54	0.09	0.55	1.0
MgO	0.9	0.2	1.1	2.6	Mg/Al	0.31	0.03	0.18	1.7
CaO	40.3	1.7	42.5	2.2	Ca/Al	16.18	3.25	0.18	91.0
Na_2O	0.1	0.02	0.2	1.6	Na/Al	0.05	0.02	0.13	0.4
K_2O	0.8	0.1	1.0	3.6	K/Al	0.38	0.02	0.34	1.1
P_2O_5	0.10	0.02	0.13	0.16	P/Al	0.025	0.004	0.008	3.2
SO_3	0.33	0.20	0.65	0.60	S/Al	0.073	0.046	0.027	2.7
As	4	3	9	10	As/Al	2.2	1.9	1.1	2.0
Ba	1285	320	1788	580	Ba/Al	699	108	66	10.7
Co	38	44	125	19	Co/Al	20.4	24.6	2.1	9.5
Cr	39	14	51	90	Cr/Al	22	10	10	2.2
Cu	84	52	164	45	Cu/Al	48.8	31.5	5.1	9.6
MnO	0.06	0.02	0.09	0.11	Mn/Al	273	88	96	2.8
Ni	87	73	225	68	Ni/Al	47.6	40.5	7.7	6.2
Rb	33	5	41	140	Rb/Al	18	1	16	1.2
Sr	623	104	743	300	Sr/Al	352	102	34	10.4
V	202	177	417	130	V/Al	111	101	15	7.5
Y	19	2	22	41	Y/Al	10.7	1.4	4.6	2.3
Zn	133	204	548	95	Zn/Al	77	124	11	77.3
Zr	32	5	40	160	Zr/Al	17	1	18	1.0
Ag	0.68	1.02	2.47	0.07	Ag/Al	0.395	0.609	0.008	49.9
Bi	0.20	0.04	0.27	0.13	Bi/Al	0.112	0.040	0.015	7.6
Cd	1.47	3.11	7.81	0.13	Cd/Al	0.869	1.884	0.015	59.1
Cs	2.2	0.3	2.6	5.5	Cs/Al	1.24	0.13	0.62	2.0
Li	15	2	17	66	Li/Al	8.0	0.6	7.5	1.1
Mo	0.4	0.6	1.5	1.3	Mo/Al	0.25	0.33	0.15	1.7
Nb	2.8	0.5	3.7	18.0	Nb/Al	1.5	0.1	2.0	0.8
Pb	12	7	26	22	Pb/Al	6.8	1.9	2.5	2.7
Re	21.9	25.7	55.1	0.5	Re/Al	12.0	14.7	0.057	210.5
Sb	0.8	1.3	3.4	1.5	Sb/Al	0.46	0.80	0.17	2.7
Sc	3	1	4	13	Sc/Al	1.9	0.1	1.5	1.3
Tl	0.69	0.48	1.23	0.68	Tl/Al	0.375	0.269	0.077	4.9
U	1.9	1.2	3.4	3.7	U/Al	1.04	0.66	0.42	2.5
TOC	1.25	1.09	2.53	0.20	-	-	-	-	-

Table 1b

Limestones (n= 42)									**LE BRECCE**
Element	conc	sigma	max	Average Shale	Element/Al	ratio	sigma	Average Shale	EF
SiO_2	15.3	7.3	56.7	58.9	Si/Al	9.06	5.97	3.11	2.9
TiO_2	0.07	0.05	0.24	0.78	Ti/Al	0.048	0.003	0.053	0.9
Al_2O_3	1.7	1.1	5.4	16.7	-	-	-	-	1.0
Fe_2O_3	0.7	0.4	2.2	6.9	Fe/Al	0.57	0.09	0.55	1.0
MgO	0.6	0.2	1.3	2.6	Mg/Al	0.44	0.13	0.18	2.5
CaO	45.0	5.0	50.9	2.2	Ca/Al	46.25	21.74	0.18	260.0
Na_2O	0.1	0.03	0.1	1.6	Na/Al	0.08	0.03	0.13	0.6
K_2O	0.4	0.2	1.2	3.6	K/Al	0.35	0.02	0.34	1.0
P_2O_5	0.05	0.01	0.08	0.16	P/Al	0.026	0.007	0.008	3.3
SO_3	0.05	0.05	0.27	0.60	S/Al	0.025	0.021	0.027	0.9
As	1	1	7	10	As/Al	1.7	2.1	1.1	1.5
Ba	513	735	3638	580	Ba/Al	491	478	66	7.5
Co	7	3	21	19	Co/Al	9.4	6.0	2.1	4.4
Cr	11	10	42	90	Cr/Al	11	5	10	1.1
Cu	14	11	70	45	Cu/Al	16.5	10.4	5.1	3.2
MnO	0.12	0.05	0.29	0.11	Mn/Al	1202	610	96	12.5
Ni	14	8	46	68	Ni/Al	15.3	3.1	7.7	2.0
Rb	15	10	51	140	Rb/Al	17	2	16	1.1
Sr	464	84	633	300	Sr/Al	635	254	34	18.7
V	22	9	60	130	V/Al	28	8	15	1.9
Y	12	4	28	41	Y/Al	15.3	4.9	4.6	3.3
Zn	22	11	60	95	Zn/Al	28	13	11	2.6
Zr	15	9	46	160	Zr/Al	16	3	18	0.9

Table 2a

Black-to-dark grey shales (n= 6)									**LE BRECCE**
Element	conc	sigma	max	Average Shale	Element/Al	ratio	sigma	Average Shale	EF
SiO_2	30.9	18.7	56.7	58.9	Si/Al	10.21	8.70	3.11	3.3
TiO_2	0.14	0.04	0.20	0.78	Ti/Al	0.050	0.002	0.053	0.9
Al_2O_3	3.1	4.4	4.4	16.7	-	-	-	-	1.0
Fe_2O_3	1.1	0.4	1.7	6.9	Fe/Al	0.45	0.06	0.55	0.8
MgO	0.7	0.2	1.0	2.6	Mg/Al	0.27	0.02	0.18	1.5
CaO	33.5	9.7	41.8	2.2	Ca/Al	14.87	4.36	0.18	83.6
Na_2O	0.2	0.1	0.4	1.6	Na/Al	0.08	0.03	0.13	0.6
K_2O	0.8	0.2	1.2	3.6	K/Al	0.38	0.38	0.34	1.1
P_2O_5	0.10	0.02	0.12	0.16	P/Al	0.026	0.004	0.008	3.3
SO_3	0.09	0.08	0.23	0.60	S/Al	0.019	0.014	0.027	0.7
As	3.0	3.3	7.0	10	As/Al	1.8	1.9	1.1	1.6
Ba	738	637	1936	580	Ba/Al	431	280	66	6.6
Co	12.2	10.4	32.0	19	Co/Al	7.4	6.8	2.1	3.4
Cr	40	21	60	90	Cr/Al	24	12	10	2.3
Cu	105	101	278	45	Cu/Al	59.2	46.1	5.1	11.6
MnO	0.05	0.02	0.08	0.11	Mn/Al	229	103	96	2.4
Ni	44	26	89	68	Ni/Al	26.8	17.1	7.7	3.5
Rb	29	9	45	140	Rb/Al	17	1	16	1.1
Sr	552	157	695	300	Sr/Al	341	91	34	10.1
V	151	121	351	130	V/Al	91	80	15	6.2
Y	14	6	23	41	Y/Al	7.8	2.7	4.6	1.7
Zn	53	17	78	95	Zn/Al	33	13	11	3.1
Zr	28	8	39	160	Zr/Al	17	1	18	0.9
Ag	0.33	0.40	1.02	0.07	Ag/Al	0.208	0.267	0.008	26.3
Bi	0.20	0.05	0.28	0.13	Bi/Al	0.126	0.045	0.015	8.6
Cd	0.28	0.20	0.67	0.13	Cd/Al	0.175	0.134	0.015	11.9
Cs	2.0	0.6	3.0	5.5	Cs/Al	1.19	0.07	0.62	1.9
Li	13	2	15	66	Li/Al	8.4	1.9	7.5	1.1
Mo	0.5	0.4	1.1	1.3	Mo/Al	0.34	0.27	0.15	2.3
Nb	2.6	0.7	3.7	18.0	Nb/Al	1.5	0.0	2.0	0.8
Pb	10	3	14	22	Pb/Al	6.2	2.0	2.5	2.5
Re	2.3	2.6	5.1	0.5	Re/Al	1.4	1.6	0.057	24.7
Sb	0.3	0.1	0.6	1.5	Sb/Al	0.18	0.10	0.17	1.1
Sc	3	1	4	13	Sc/Al	1.9	0.1	1.5	1.3
Tl	0.29	0.06	0.36	0.68	Tl/Al	0.176	0.024	0.077	2.3
U	1.6	0.8	2.3	3.7	U/Al	0.98	0.46	0.42	2.3
TOC	0.75	0.64	1.67	0.20	-	-	-	-	-

Table 2b

MONTE PETRANO					
Samples MP1, MP2, MP6			**Samples MP3, MP4, MP5**		
Element/Al	EF	EF sigma	Element/Al	EF	EF sigma
Mn/Al	3.4	0.9	Mn/Al	2.3	0.5
Re/Al	0.0	0.0	Re/Al	421.1	183.6
V/Al	2.1	1.1	V/Al	13.1	5.1
Cd/Al	2.9	3.0	Cd/Al	115.3	177.6
Ag/Al	5.6	4.9	Ag/Al	94.2	94.2
Cu/Al	9.6	2.8	Cu/Al	8.6	8.9
Ni/Al	2.7	0.7	Ni/Al	9.5	5.9
Mo/Al	0.4	0.4	Mo/Al	2.9	2.8
U/Al	1.2	0.4	U/Al	3.8	1.0
Zn/Al	2.0	0.8	Zn/Al	12.2	16.1
Pb/Al	2.2	0.9	Pb/Al	3.2	2.7
As/Al	0.8	1.0	As/Al	3.1	1.5
Cr/Al	2.0	1.2	Cr/Al	2.2	0.8
Co/Al	3.3	2.4	Co/Al	6.9	14.4
Fe/Al	1.0	0.1	Fe/Al	1.0	0.2
S/Al	1.5	0.2	S/Al	3.9	1.6
	average	sigma		average	sigma
TOC	0.29	0.20	TOC	2.22	0.40

LE BRECCE					
Samples BR1, BR2, BR6			**Samples BR3, BR4, BR5**		
Element/Al	EF	EF sigma	Element/Al	EF	EF sigma
Mn/Al	2.7	1.3	Mn/Al	1.2	0.6
Re/Al	0.0	0.0	Re/Al	49.4	13.7
V/Al	2.7	1.8	V/Al	9.3	6.0
Cd/Al	7.3	1.7	Cd/Al	16.4	12.0
Ag/Al	5.8	6.2	Ag/Al	46.7	39.2
Cu/Al	10.6	11.2	Cu/Al	12.8	8.6
Ni/Al	2.2	0.5	Ni/Al	5.3	3.0
Mo/Al	3.4	1.9	Mo/Al	1.3	1.3
U/Al	1.9	0.6	U/Al	3.2	0.6
Zn/Al	8.1	8.1	Zn/Al	3.9	1.0
Pb/Al	2.7	0.6	Pb/Al	2.4	0.8
As/Al	0.3	0.5	As/Al	3.0	1.2
Cr/Al	1.7	1.1	Cr/Al	3.1	1.1
Co/Al	2.2	1.4	Co/Al	4.6	4.4
Fe/Al	0.8	0.1	Fe/Al	0.8	0.1
S/Al	0.9	0.7	S/Al	0.5	0.2
	average	sigma		average	sigma
TOC	0.30	0.28	TOC	1.20	0.59

Table 3

Local background		
(Element/Al)bg	**MONTE PETRANO**	**LE BRECCE**
Si/Al	3.95	4.30
Ba/Al	79	55

Table 4